Supplementary Information for

High Throughput Exsolution Design of CO_2 Reduction Reaction Interface in a Copper/High-Entropy Oxide Tandem Electrode

ShengQuan Xuan[1#], Tamilselvi Gurusamy[2,3,4#], Xin Wang[1,5#], Hui Zheng[6], Huiming Guo[1], Hasti Vahidi[1], Alexander D. Dupuy[1,7], Liela Clarke[1,8], Julie M. Schoenung[1,9], Shyue Ping Ong[6], Hang Ren[2,3,4*], William J. Bowman[1*]

[1] Department of Materials Science and Engineering, University of California, Irvine, Irvine, CA 92617
[2] Department of Chemistry, The University of Texas at Austin, Austin, TX 78712
[3] Center for Electrochemistry, The University of Texas at Austin, Austin, TX 78712
[4] Texas Materials Institute, The University of Texas at Austin, Austin, TX 78712
[5] Department of Metallurgical and Materials Engineering, University of Alabama, Tuscaloosa, AL 35487
[6] Chemical and Nano Engineering, University of California, San Diego, La Jolla, CA 92093
[7] Department of Materials Science and Engineering, University of Connecticut, Storrs, CT 06269
[8] Department of Chemical Engineering, Rowan University, Glassboro, NJ 08028
[9] Department of Materials Science and Engineering, J. Mike Walker '66 Department of Mechanical Engineering, Texas A&M University, College Station, TX 77840

[#] Equal contribution author

* Corresponding authors: William J. Bowman will.bowman@uci.edu, Hang Ren hren@utexas.edu

Supplemental Note Contents

Note S1. Methods

1.1. Demonstrating P(O_2) controlled growth of entropy stabilized oxide (ESO)-based thin film nanocomposite with Cu nanorods

1.1.1. ESO-based thin film preparation

The single-phase rocksalt ($Mg_{0.2}Co_{0.2}Ni_{0.2}Cu_{0.2}Zn_{0.2}$)O entropy stabilized oxide (ESO) PLD ablation target was fabricated by ball milling of the five constituent oxide nanopowders (US Research Nanomaterials Inc., TX, USA) in equimolar amounts, followed by conventional sintering at 900 °C for 2 hours. Details of the target synthesis procedures can be found in our previous work[1].

ESO-based thin films were prepared by pulsed laser deposition (PLD) using a Nd:YAG solid laser with 266 nm wavelength and 10 ns pulse duration (Continuum SL III-10) and a high-vacuum deposition system (Neocera Pioneer 180 GLAD PLD System). (001) Si wafers (MTI Corporation) were used deposition substrates after a cleaning sequence of in acetone, isopropanol and methanol. The substrate–target separation was 57 mm. For non-gradient PLD, the substrate temperature was 300°C and a fixed laser energy fluence of 5.3 mJ/cm^2 was used by setting a voltage for laser excitation of 1.4 kV. The oxygen pressure during PLD deposition was conrtolled by regulating the flow rate of the inlet high purity O_2 gas (99.994%). With O_2 flow rates increase from 0 and 50 sccm, the deposition pressure were found to increase from 0.03 to 0.63 mtorr.

Single-layer low P(O_2) and high P(O_2) thin films were deposited under P(O_2) of 0.03 and 0.63 mtorr, respectively, for 40,000 pulses. Bi-layer thin films were deposited under P(O_2) of 0.03 mtorr for 10,000 pulses and under P(O_2) of 0.63 mtorr for 30,000 pulses. For heat treatment study, 4-layer thin films was deposited under P(O_2) of 0.03, 0.63, 0.03 and 0.27 mtorr. Heat treament of the 4-layer films were carried out in the PLD chamber at 600°C for 2 hours under controlled P(O_2) of 0.03 mtorr and 0.57 torr, respectively. To show the effect of P(O_2) over the 0.03-0.63 mtorr range, a 11-layer film was deposited under a P(O_2) sequence of 0.03-0.63-0.03-0.51-0.03-0.39-0.03-0.27-0.03-0.15-0.03 mtorr and for 10,000 pulses for each layer.

1.1.2. Microstructure characterization

Phase and crystallographic structure analysis of the ESO target and thin films was characterized using an X-ray diffractometer (SmartLab, Rigaku, Tokyo, Japan) with Cu-Kα X-ray radiation. X-ray diffraction (XRD) patterns of the ESO target pellet and ESO-based thin films were collected with para-focusing beam at a symmetric θ-2θ geometry and parallel beam under grazing incidence diffraction geometry, respectively.

Scanning transmission electron microscope (STEM) was performed with the JEOL JEM-ARM300F Grand ARM operated at 300 kV equipped with dual silicon drift detectors for energy-dispersive X-ray spectroscopy (EDS) and the Gatan K2 IS/summit for counting EELS. Transmission electron microscopy (TEM) and selected area electron diffraction (SAED) were carried out on a JEOL JEM-2800 at an operating voltage of 200 kV. The cross-sectional and plane-view TEM specimens of the ESO-based thin films were fabricated by focused ion beam (FIB) using a FEI Quanta 3D FEG dual-beam FIB-SEM.

In situ annealing experiment on the 4-layer thin film was perfored inside the JEOL JEM-ARM300F Grand ARM using a Gatan heating holder. The temperature was ramped from room temperature to 120°C, 300°C, 400°C and then 500°C at a rate of 20°C/min with a ~15-min hold at each temperature for STEM imaging and EELS.

1.1.3. Conductivity measurement

An EMS 150T sputter coater was used to coat two ~ 30nm thick Ir electrodes on top of each thin film. Temperature-dependent cyclic voltammetry (CV) measurements of the thin films were carried out by a Biologic sp-200 electrochemical workstation associated with Linkam probe stage (HFS600E-PB4) and Linkam temperature controller (T96 System Controller). The CV measurements were obtained using a two-probe measurement. Measurements were conducted in ambient air and synthetic dry air (to ensure this effect was not related to moisture adsorption from the environment) over the temperature range of 25-200 °C. Measurements were repeated 3 times to verify repeatability. Samples were equilibrated at each temperature for 30 min before the data was measured.

1.1.4. DFT Computational simulation

All the density functional theory (DFT) calculations were performed using the Vienna Ab initio Simulation Package (VASP)[2] within the projector augmented-wave approach (PAW)[3]. The Perdew-Burke-Ernzerhof (PBE) generalized-gradient approximation (GGA) functional[4] was used for all the relaxations and static calculations. We considered on-site Coulomb interaction correction via DFT + Hubbard U formalism. The U values were selected via pymatgen[5] MPRelaxSet/MPStaticSet[6], in which U values of 3.32 and 6.2 eV for Co and Ni, respectively. The surface structures are generated via pymatgen[5]. As the ground states for NiO and CoO are antiferromagnetic (AFM), the lowest magnetic configurations were selected and obtained from the Materials Project database API[6,7]. For NiO and CoO, (100) and (110) surfaces we considered AFM configuration, while for (111) surfaces, only ferromagnetic configurations are considered due to the large cell size/number of atoms in the cell.

1.2. High-throughput tandem electrode synthesis and characterization

1.2.1. Electrocatalytic Tandem electrode (ESO-Cu) synthesis

Tandem electrode (ESO-Cu) was also fabricated using the same PLD target, PLD system, substrate, and substrate preparation method as mentioned above. However, PLD synthesis parameter and substrate geometry were different. Two Si chips were overlayed with 7 mm offset and adhered to PLD heating plate to introduce deposition temperature gradient during the PLD (**Fig. S12-S13).** The substrate heater temperature was set 375 °C, laser fluence of 5.3 mJ/cm^2 was introduced by setting laser excitation voltage of 1.38 kV, and oxygen pressure was set to 0.015 mtorr by controlling turbo pump speed. 40,000 pulses at 10 Hz were deposited after the desired environment conditions were met. After the deposition, the heating plate is cooled in same vacuum condition until it reaches room temperature, and subsequently the chamber was vented to take sample out.

1.2.2. Microstructure characterization

XRD and STEM EDS were done using the same instruments as mentioned in P(O_2) varying case. θ-2θ Bragg-Brentano geometry was used, and divergent slits were chosen as such that only part of thin film was scanned (**Fig. S13b**). The same acceleration voltage and detector were used for STEM EDS data collection as in the P(O_2) varying study. SEM imaging and STEM sample preparation were done using SEM FIB (Tescan GAIA3). Select regions where SEM imaging and STEM sample preparation took place on gradient film are also pointed out in **Fig. S13b**. SEM images used for grain size measurement are displayed in **Fig. 14**. XPS data was acquired using

AXIS Supra by Kratos Analytical at Ultra-high vacuum using Al-K α as X-ray source. Exposed scan area for XPS is also displayed in **Fig. S13b.**

1.2.3. Temperature gradient simulation

The transient thermal module of Ansys was used to simulate the lateral temperature gradient profile of the Si substrate. Si thermal conductivity was acquired from Shanks *et al.*[8], specific heat from NIST workbook[9], and convection coefficient from Timans *et al.*[9]. The simulation had three intervals with different time steps for optimal simulation results (**Table S1-S2**).

Table S1. Time intervals and steps used for optimal temperature gradient simulation.

Order of interval	Time interval (s)	Time step (s)
1st	0 - 3	5×10^{-2}
2nd	3 - 500	1
3rd	500 - 3000	5

Table S2. Transient thermal simulation of the PLD substrate temperature gradient.

Distance from hot edge of gradient (mm)	Simulated Temperature (°C)
0.5	369
1.5	368
2.5	360
3.5	333
4.5	304
5.5	282
6.5	265
7.5	254
8.5	245
9.5	241

1.2.4. SECCM experiments: Fabrication of probe, electrode, and experimental conditions

The nanopipettes used in this study were prepared from Quartz glass, having an outer diameter of 1.0 mm, an inner diameter of 0.7 mm, and a length of 7.5 cm. To fabricate the pipette, the CO_2 laser puller from Shutter Instrument Co. (model P-2000) was used, taking on specific pulling parameters: heat=480, Fil=1, Vel=30, Del=145, Pul-200, line=1, and prog=5. The pulled nanopipette tip showed an opening diameter of approximately 500 nm (SEM image shown in **Fig.**

S27). To act as a probe, the nanopipette was filled with a 10 mM $KHCO_3$ electrolyte. Moreover, to prevent evaporation of the electrolyte, silicon oil was added at the top of the electrolyte. The quasi-reference counter electrode, Ag/AgCl, was prepared by immersing an Ag wire into a NaClO solution to deposit Cl. The prepared Ag/AgCl wire was then inserted into the top of the nanopipette, positioned approximately 3-4 cm away from the tip end. The movement across various positions on the tandem Cu-ESO electrode was achieved by the Piezo Motor Controller from THORLABS, specifically the Single-Channel K-cube inertia motor controller (KIM001). This controller was coupled with Piezoelectric Inertia Actuators featuring a 25 mm travel mounting barrel (KPS201).

Electrochemical experiments were executed using Labview software. Given the gas-dependent nature of the study, a closed cell setup was used to maintain a saturated environment with a specific gas (**Fig. 5a**). To ensure the gas saturated environment, humidified CO_2 gas, of research-grade purity (99.999 %), was consistently supplied at a rate of 40 mL/min throughout the experiment. To make sure, sufficient saturation, 30 minutes prior to beginning the experiment, a gas was supplied into the electrochemical cell. A small opening at the top of the cell served a dual purpose – facilitating the movement of the nanopipette across the sample and helps for gas outlet. For the control study, N_2 gas was saturated similarly to CO_2. All presented results are referenced to the RHE scale.

To convert the potential to RHE, the formula $E(RHE) = E(Ag/AgCl) + E^0(Ag/AgCl) + 0.0591pH$ was employed. Here, E(Ag/AgCl) represents the observed potential, and $E^0(Ag/AgCl)$ is + 0.69 (at pH 8.3), equivalent to +0.2 (at pH=0), serving as the standard potential of the quasi-reference electrode potential. This was determined by conducting cyclic voltammetry on a Pt ultramicroelectrode in an H_2-saturated electrolyte solution (10 mM $KHCO_3$). The pH of the N_2-saturated and CO_2-saturated electrolytes were measured to be 8.4 and 5.9, respectively.

1.2.5 EELS multiple linear least squares (MLLS) fitting

MLLS fitting technique within Gatan Digital Micrograph software was used for EELS Cu $L_{2,3}$ edge oxidation mapping. Reference standard EEL near-edge fine structure spectra are acquired either from part of the sample under analysis or from a different sample with known oxidation state. Standards for $Cu^{1+}{}_2O$, and $Cu^{2+}O$ are acquired from nanopowders from US Research nanomaterials Inc. The XRD data of these standard nanopowders are plotted with references in **Figs. S23-S24** for $Cu^{2+}O$ and $Cu^{1+}{}_2O$ respectively to ensure credibility of these standards. The Cu^0 spectrum is taken from within our data where the highest agglomeration of Cu signal is and there is absence of EELS signal from oxygen and other elements. Our Cu^0 standard was compared against the EELS Atlas database[10] to confirm it is Cu^0 (**Fig. S25**). An EEL spectral background standard at Cu $L_{2,3}$ region is also needed for MLLS, especially for data points with low Cu signal intensity. An example of optimal fitting is shown in **Fig. S26** for a combination of $Cu^{1+}{}_2O$**,** Cu^0, and background standards.

Note S2. Effects of $P(O_2)$ on Cu-ESO film structure and nanorod morphology

$P(O_2)$ is an important thermodynamic parameter determining the surface energy landscape for the films' nucleation and growth. During PLD growth, the plasma plume containing the ablated ions reach the substrate surface in microseconds, followed by a relatively long relaxation period[11]. $P(O_2)$ plays an important role in both mechanisms and therefore strongly affects the stoichiometry, crystallization, texture, microstructure, and properties of thin films. At low $P(O_2)$, the ions have higher diffusion mobility, resulting in nucleation and coalescence of Cu-rich metal clusters, which can act as heterogeneous nucleation sites for metal adatoms, leading to the formation of near vertically aligned metal rods[11]. Change in the relative SAED peak intensities under different $P(O_2)$ growth reveals the polycrystalline texture is affected by this processing parameter (**Fig. S1**).

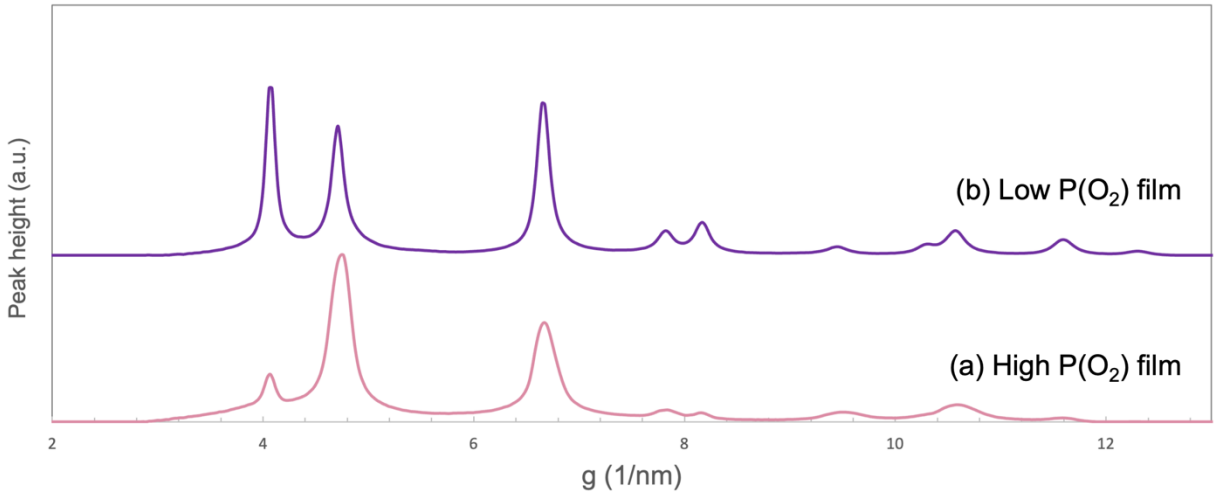

Fig. S1. Radial peak intensity profiles[12] for selected area diffraction patterns (SAEDs). (a) High $P(O_2)$ film (0.63 mtorr) and **(b)** low $P(O_2)$ film (0.03 mtorrr).

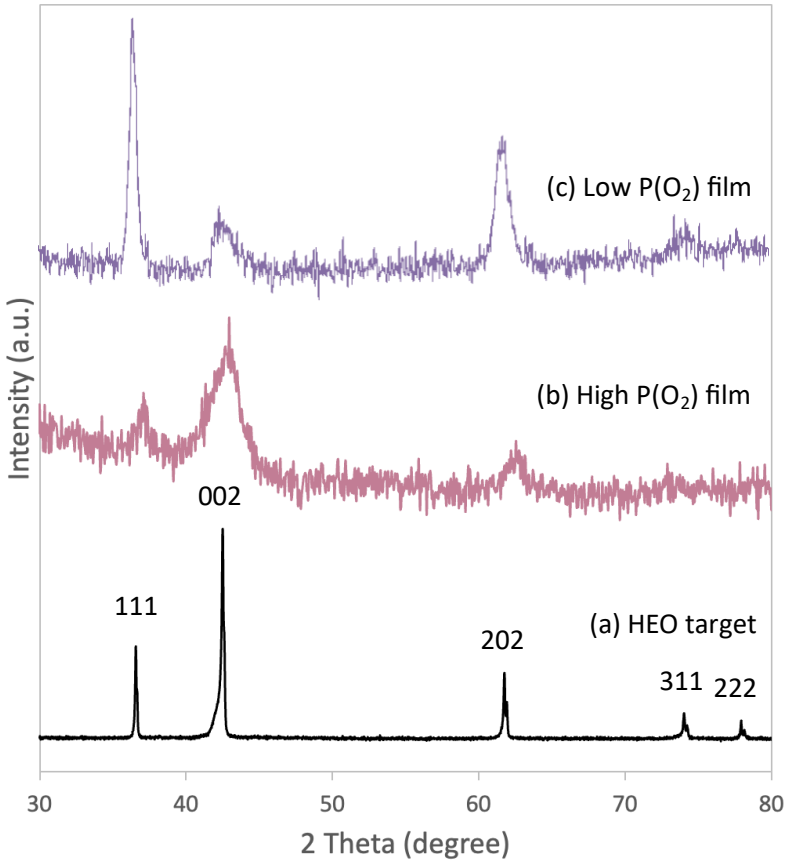

Fig. S2. X-ray diffraction (XRD) patterns. (**a)** The bulk ESO target and the ESO-based thin films deposited under **(b)** high $P(O_2)$ (0.63 mtorr) and **(c)** low $P(O_2)$ (0.03 mtorrr).

Nanorod tilting angles range from 0-25 ° (**Fig. S3**), with high aspect ratios of ~13. This is consequential as aligned metal nanorods with large aspect ratios provide extremely anisotropic magnetic[13] and photonic[14] properties.

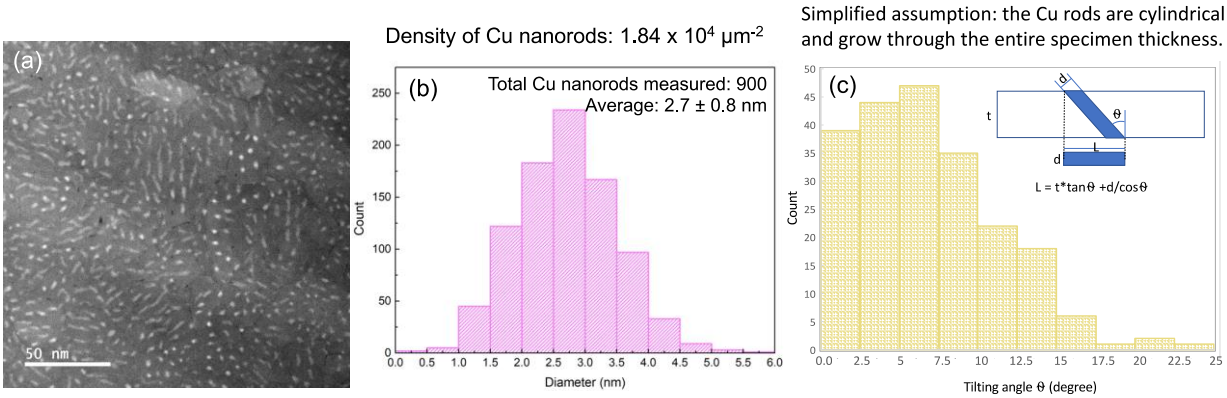

Fig. S3. Statistical analysis of the size and orientation of the Cu nanorods. (a) A representative in-plane high angle annular dark field (HAADF) STEM image of the low $P(O_2)$ film showing a high density of Cu nanorods. **(b)** Histogram of the diameter distribution of the Cu nanorod. **(c)** Estimated tilting angle distribution of the Cu nanorods relative to the thin film normal direction.

Note S3. Multilayer films deposited at different $P(O_2)$

In a bilayer film, all five cations are homogeneously distributed in the high $P(O_2)$ 0.63 mtorr layer (**Fig. S4a**), whereas in the low $P(O_2)$ 0.03 mtorr layer Cu-rich metal nanorods form which lowers the ESO concentration Cu from 20 at. % to ~ 7.9 at. % (**Table S3**). A continuous and coherent Cu-rich layer ~ 2 nm thick is formed interface between the two layers, indicating rapid Cu diffusion to the film surface under the low $P(O_2)$ condition (**Fig. S4b-c**). The Cu-rich layer shows an epitaxial relationship with the low and high $P(O_2)$ layers, which allows columnar grain growth continuously across the interface.

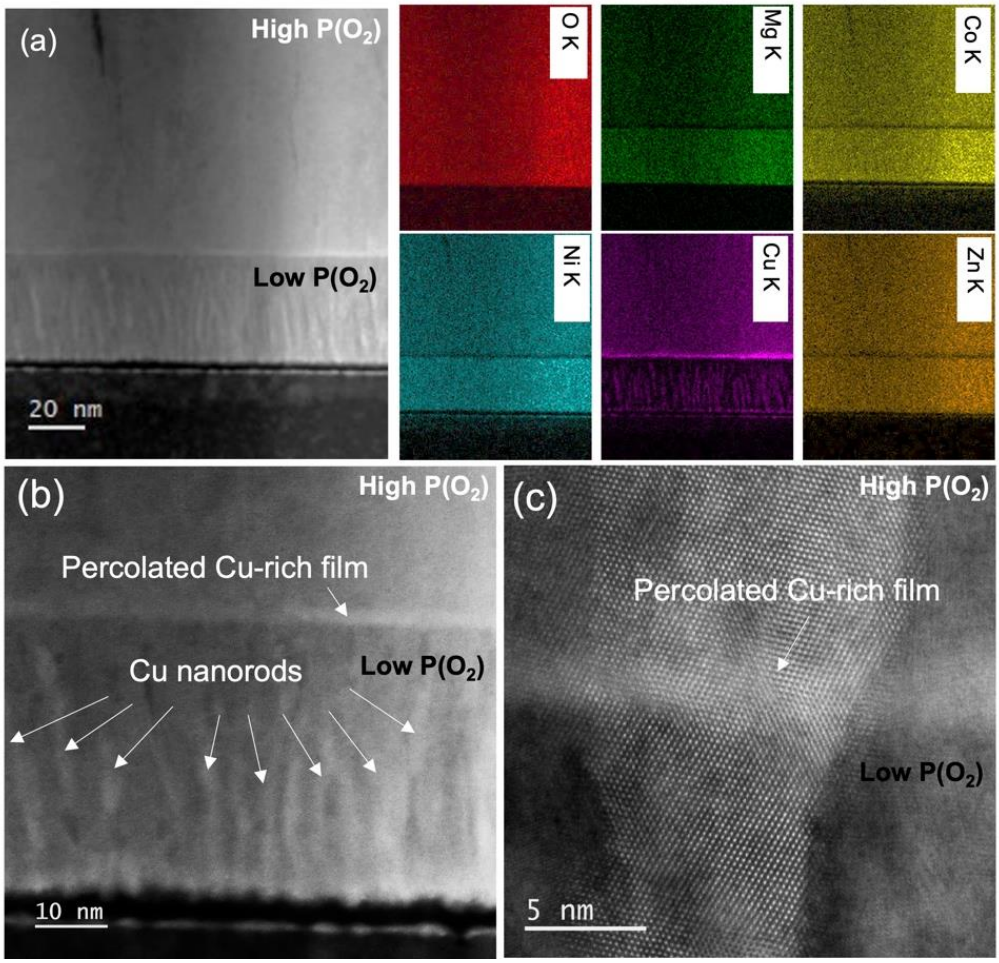

Fig. S4. Structure of a bi-layer stacked low $P(O_2)$-high $P(O_2)$ layer/film. (a) ADF STEM image of a bi-layer thin film deposited under 0.03 and 0.63 mtorr for the bottom and top layer, respectively, and the corresponding STEM EDS maps. **(b,c)** low and high magnification ADF STEM images near the bi-layer interface.

Table S3. Chemical composition in the low $P(O_2)$ film measured by STEM EDS.

X-ray line	Average cation concentration (at. %)
Mg K	28.14 ± 0.32
Co K	23.24 ± 0.20
Ni K	21.86 ± 0.41
Cu K	7.92 ± 0.17
Zn K	18.84 ± 0.23

*The Cliff–Lorimer factors (k-factors) used for EDS quantification are manually calculated by assuming the atomic percentage for each cation in the high $P(O_2)$ film is 20%.

The O K, Co $L_{2,3}$, Ni $L_{2,3}$ and Cu $L_{2,3}$ energy loss near-edge structure (ELNES) revealed that the O K edge pre-peak disappears in the low P(O_2) layer (**Fig. S5a-c**), owing to the reduction of the neighboring transition metals or the formation of oxygen vacancies[15]. The ratio of the Co L_3 to L_2 white lines appears higher in the low P(O_2) layer and lower in the high P(O_2) layer (**Fig. S5d**), corresponding to changes in the Co oxidation states, with an estimated average valence states of +2.9 to +2.5 in the high P(O_2) and low P(O_2) layer, respectively[16]. Despite differences in intensities, the $L_{2,3}$ ELNES of Ni (**Fig. S5e**) is similar to that reported for Ni^{2+} in NiO[17,18]. Both Co and Ni show higher concentrations at low P(O_2) than that at high P(O_2) and the lowest concentrations at the interface. Cu $L_{2,3}$ edges show changes in both intensity of the white lines and the post-edge continuum with a change in P(O_2), indicating significant changes in Cu concentrations within the bilayer film and the formation of Cu^0 in the low P(O_2) layer and at the interface[19] (**Fig. S5f**).

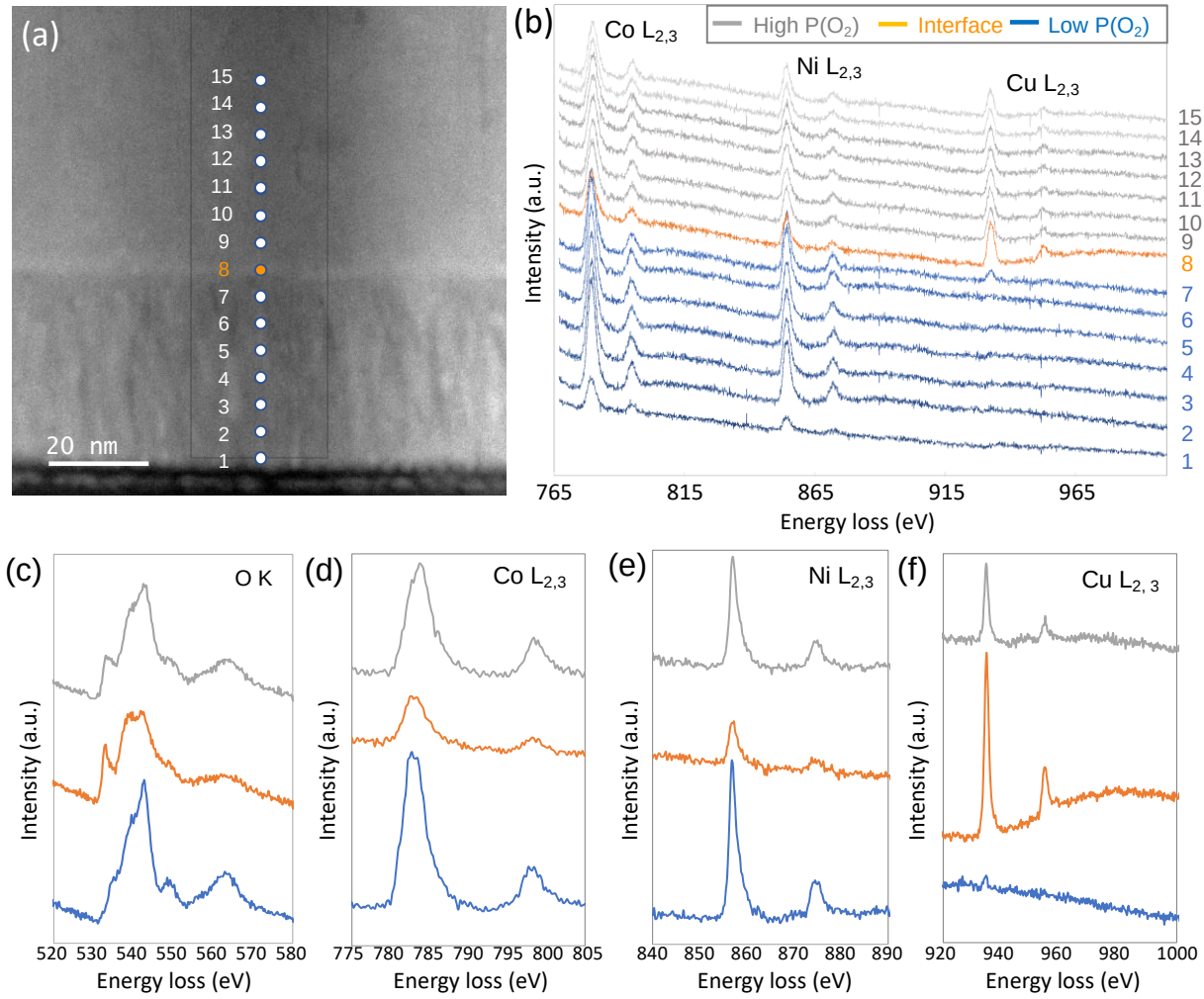

Fig. S5. Chemical states of elements in a bilayer ESO film from STEM EELS. (a,b) STEM EELS spectra as a function of sampling locations, showing changes in Cu concentration and Co oxidation states in bi-layer ESO thin film across the horizontal interface. **(c-f)** Core loss electron loss near-edge structure (ELNES) spectra for O K-, Co L-, Ni L- and Cu L-edges.

To explore and understand the relevant growth conditions for nanocomposite ESO film, we have deposited 11-layer thin films under varying $P(O_2)$ (**Fig. S6a-h**). Our experiments show that Cu-rich metal nanostructures are not formed at $P(O_2)$ of 0.15 mtorr or higher, but lower $P(O_2)$ slightly reduces the Cu concentration in the thin films (**Fig. S6i**).

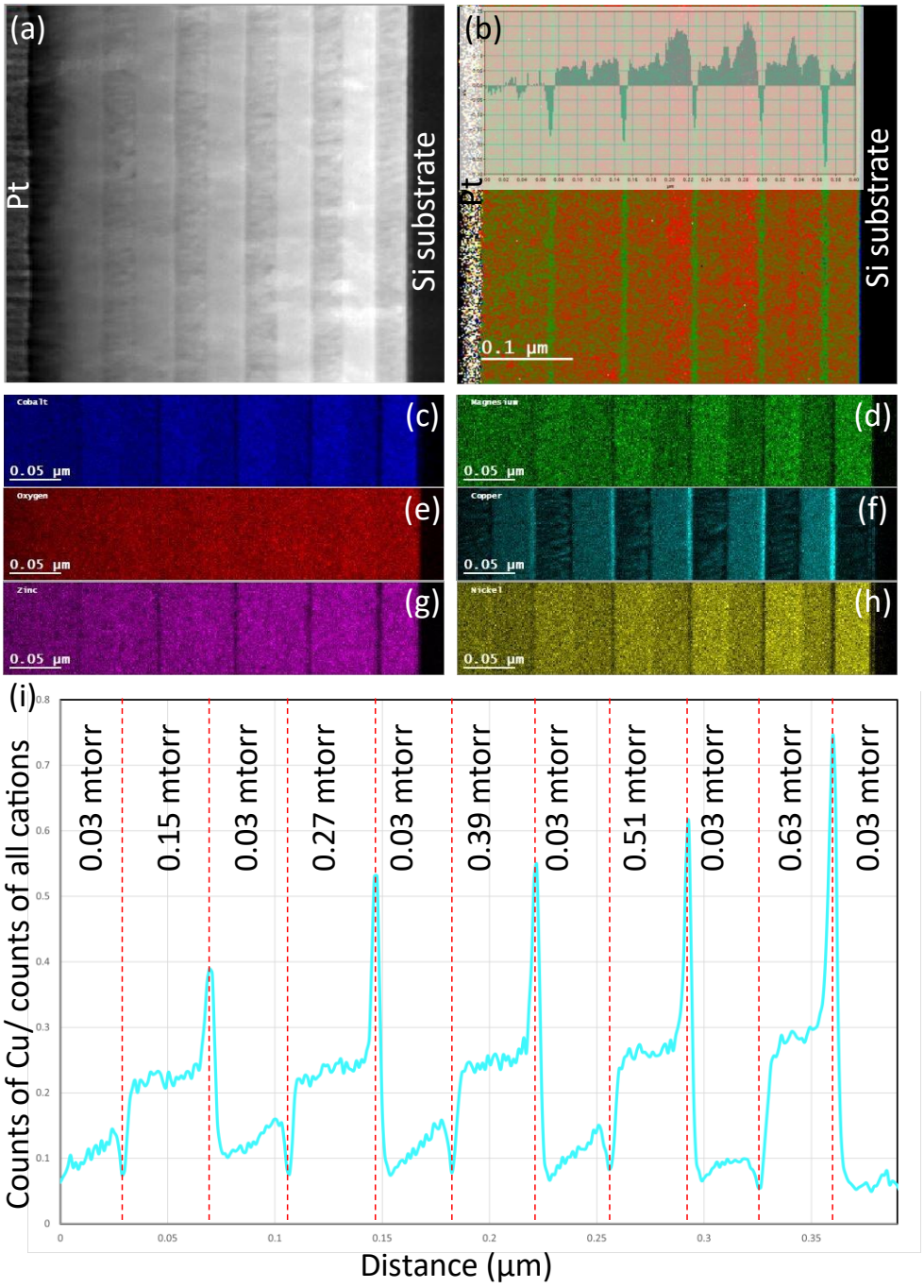

Fig. S6. Microstructure and composition analysis of a 11-layer thin film deposited under varied $P(O_2)$ conditions. (a) A bright field STEM image. **(b)** EELS peak shift map of the plasma peak at ~21 eV relative to the 0.15 mtorr layer, with red color representing positive peak shift and green color representing negative peak shift. Inset is the profile of the peak shift, demonstrating obvious plasma peak shifts of -0.22 ~ -0.35 eV at the location of the Cu-rich percolation films. **(c-**

h) STEM EDS maps of the 11-layer film showing Cu-rich nanorods are only formed when $P(O_2)$ is 0.03 mtorr with Cu-rich percolation films formed on top of the 0.03 mtorr layers. **(i)** Profile of Cu K signal in counts normalized by the sum of signals for all cations.

Note S4. Post-mortem and in situ STEM characterization of heat-treated ESO thin films

The nanocomposite structure is not thermodynamically stable, with ~ 50 - 100 nm sized Cu-rich equiaxed nanograins formed after annealed at 600 °C for 2 hours under $P(O_2)$ of 0.57 torr (**Fig. S7**) and 0.03 mtorr (**Fig. S8**), respectively. A similar microstructural evolution has been recently reported in a NiO:$La_{0.7}Sr_{0.3}MnO_3$ system, where the NiO phase changed from cylindrical to spherical shape after annealed in vacuum[20]. The evolution of the microstructure during annealing can be driven by the minimization of the high strain energy in the vertical interface[20]. Interestingly, in situ heating inside TEM shows that Cu-rich nanorod structure were observed in both the low $P(O_2)$ and high $P(O_2)$ layers at 400 °C, suggesting that the formation of Cu-ESO nanocomposite structure might be thermodynamically driven under the extremely low $P(O_2)$ condition inside the TEM chamber (**Fig. S9**).

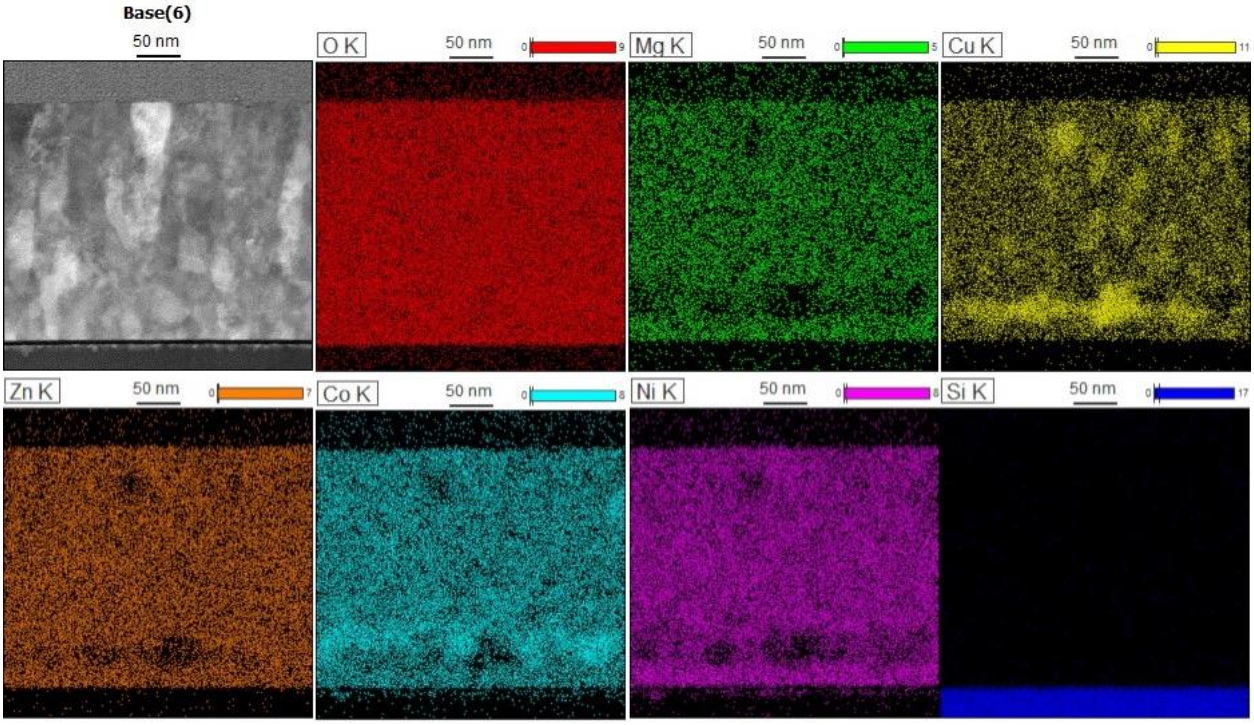

Fig. S7. Microstructure and chemistry of the multi-layer ESO film after heat treatment at 600°C under $P(O_2)$ of 0.57 torr for 2 hours.

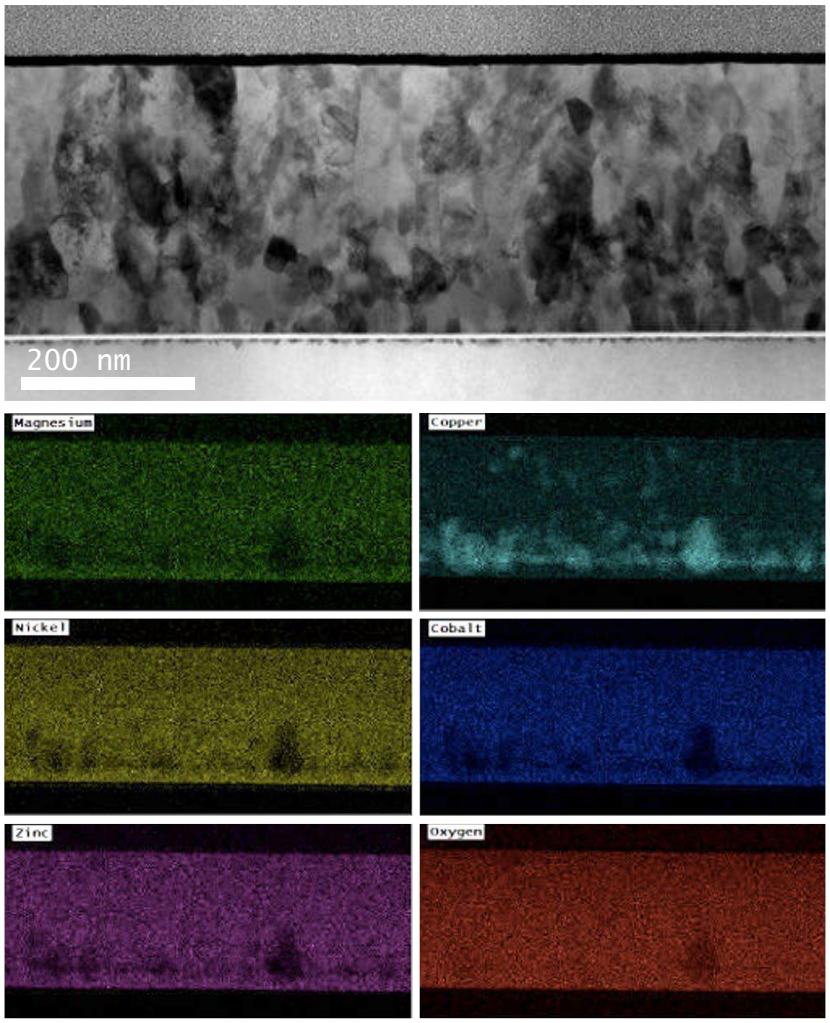

Fig. S8. Microstructure and chemistry of the multi-layer ESO film after heat treatment at 600°C under P(O_2) of 0.03 mtorr for 2 hours.

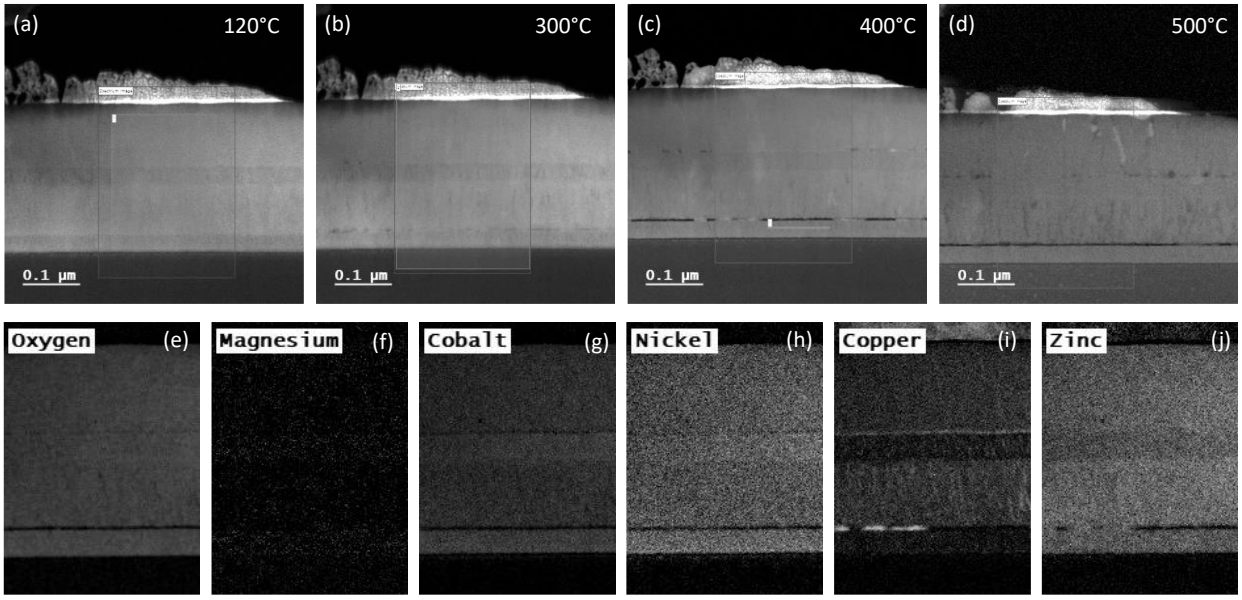

277
278 **Fig. S9. In situ heating results of the 4-layer ESO. (a-d**) HAADF STEM images taken at 120 °C,
279 300 °C, 400 °C and 500 °C, respectively. **(e-j)** EELS maps for O, Mg, Co, Ni, Cu, Zn, respectively,
280 at 400 °C.

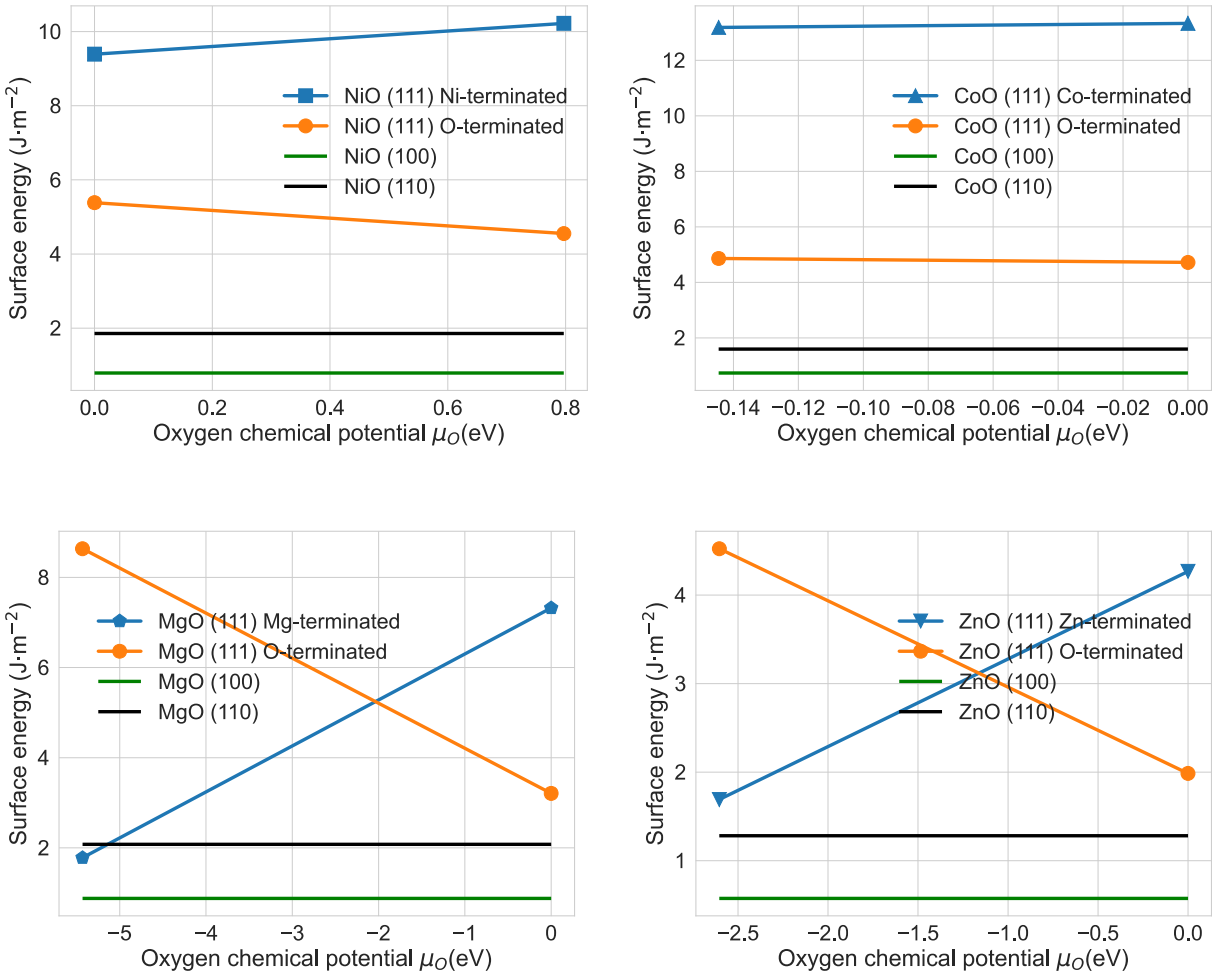

Fig. S10. The surface energies for constituent metal oxides NiO, CoO, MgO, and ZnO, assuming the ESO's rocksalt structure, as a function of oxygen chemical potential μ_O. Stoichiometric surface (100) corresponds to the lowest energy for all the constituent metal oxides.

Table S4. Surface energies calculated in this work and those from the literature.

	This work	Literature		
Composition	Surface energy ($J \cdot m^{-2}$)	Structure	Surface plane	Surface energy ($J \cdot m^{-2}$)
MgO	0.88	rocksalt	(100)	1 [21]
MgO	0.88	rocksalt	(100)	0.89 [22]
CoO	0.74	rocksalt	(100)	1.66 [23]
CoO	0.74	rocksalt	(100)	0.8 [24]
NiO	0.79	rocksalt	(100)	0.95 [25]
NiO	0.79	rocksalt	(100)	0.6 [26]
CuO	0.34	monoclinic	(010)	1.04 [27]
ZnO	0.57	rocksalt	(100)	0.63 [22]
MgO	2.08	rocksalt	(110)	2.29 [28]
MgO	2.08	rocksalt	(110)	2.17 [22]
CoO	1.6	rocksalt	(110)	2.57 [23]
NiO	1.85	rocksalt	(110)	2 [25]
CuO	1.04	monoclinic	(110)	1 [29]
ZnO	1.28	rocksalt	(110)	1.52 [22]

Note S5. Electronic conductivity mechanism of ESO and Cu-ESO thin films

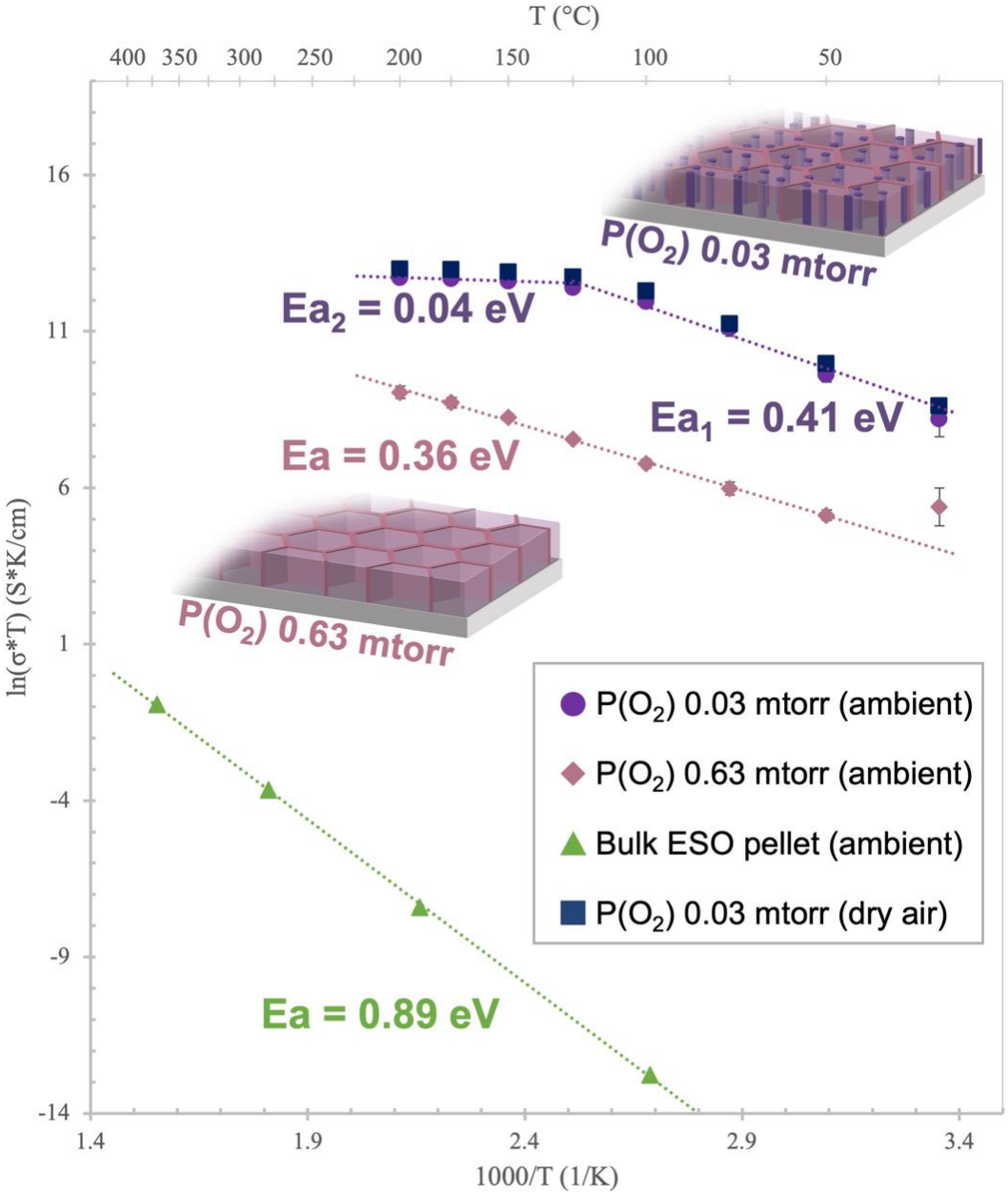

Fig. S11. Electrical conductivity. Arrhenius plots of measured in-plane conductivity for the bulk ESO ceramic pellet used as the PLD precursor (green), the films deposited under $P(O_2)$ of 0.03 and 0.63 mtorr measured under laboratory air, and the 0.03 mtorr sample measured under dry synthetic air.

The ESO PLD precursor was measured in ambient air, with E_a = 0.89 eV. Our recent work[30] showed that electrical conductivity in this ESO results from electronic conduction via Cu^{+}/Cu^{2+} small polaron hopping. The polycrystalline 0.63 mtorr film's conductivity increased by 5 orders of magnitude from 2.8 x 10^{-4} S/cm to 18 S/cm in ambient air at 200 °C, with corresponding decrease in E_a to 0.36 eV. Similar to E_a values that have been previously reported[31,32], conduction is attributed to electronic small polaron hopping between Cu^{2+}/Cu^{+} and Co^{3+}/Co^{2+} mixed-valence cation pairs. Unlike the precursor, which was annealed under oxidizing conditions, this film

(grown at 0.63 mtorr) is expected to have a higher concentration of oxygen vacancies charge-compensated by Cu^{2+} and Co^{2+} reduction (e.g., $O_O^{\times} + 2Cu_{Cu}^{\times} \leftrightarrow V_O^{\bullet\bullet} + 2Cu'_{Cu}$). Additionally, the film's smaller grain size (10 - 15 nm) compared to the pellet (~ 2 μm) increase the grain boundary area, where Cu segregation and valence reduction are expected—which we have shown increase the electronic conductivity through the ESO grains [30]. The film growth at 0.03 mtorr yielded Cu nanorod formation throughout the ESO film, further increasing electronic conduction and inducing an unexpected polaron-polaron transition at 100 °C where E_a abruptly changes from 0.41 eV (< 100 °C) to 0.04 eV (> 100 °C).

Along with increasing the Cu^{2+} valence reduction by lowering the growth $P(O_2)$, nanorod formation significantly reduces the Cu concentration in the oxide, which is thought to (i) introduce Cu cation vacancies, V''_{Cu}, charge compensated by $V_O^{\bullet\bullet}$ (**Fig. 1g**) and (ii) oxidize some Co^{2+} to Co^{3+} ($Co^{\bullet}_{Co}$) and some Ni^{2+} to Ni^{3+} ($Ni^{\bullet}_{Ni}$). As the redox energy of the Co and Ni pairs are similar, both are considered here assuming that the couples' redox energy ranges are spread via perturbations in periodic site potentials and elevated disorder in the ESO[33]. Therefore, the increased conductivity and modest change in E_a compared to the 0.63 mtorr film below 100 °C is attributed to added Cu^{2+}/Cu^{+}, Co^{2+}/Co^{3+}[32], and Ni^{2+}/Ni^{3+}[34] polaron hopping pairs. Surprisingly, electron conductivity above 100 °C exhibits E_a of 0.04 eV—reminiscent of high-mobility Ni^{2+}/Ni^{3+} polaron transport in the perovskite $I.a_{1-x}Sr_xCo_{1-y}Ni_yO_{3-\delta}$[33] and high-mobility polaron transport between Co^{3+} spin states in the perovskite $LaCoO_3$[35]; the motional enthalpies (a component of E_a) in those oxides are 0.03 eV and 0.05 eV, respectively. The polaron-polaron transition, from relatively high-E_a conduction via Cu^{2+}/Cu^{+} pairs (< 100 °C) to low-E_a conduction (> 100 °C), is thought to arise from a combination of two effects: (i) Greater Ni^{3+}-O covalency—which increases with Ni-O-Ni bond angle distortion and was identified as the origin of metallic conductivity in $LaNiO_3$[33,36]; bond distortion in this ESO increases with $V_O^{\bullet\bullet}$ content[37] and is assumed to increase with temperature here. And (ii) stabilization of an ordered mixture of low- and high-spin-state Co^{3+}—which occurs below ~100 °C in $LaCoO_3$ and facilitates high-mobility polaronic transport between Co^{3+} sites[35]; as the ratio of low/high spin states is stabilized by temperature-dependent dynamic ordering[35] it is hypothesized that 100 °C corresponds to the onset of percolation in the ESO film here. To summarize, low-E_a (0.04 eV) conduction above 100 °C is attributed to high-mobility polaronic transport due to greater Ni^{3+}-O covalency caused by temperature-dependent Ni-O-Ni bond distortion and the stabilization of mixed spin state Co^{3+} sites above 100 °C, which together form a percolating transport path.

Note S6. Gradient substrate temperature PLD and tandem electrode characterization

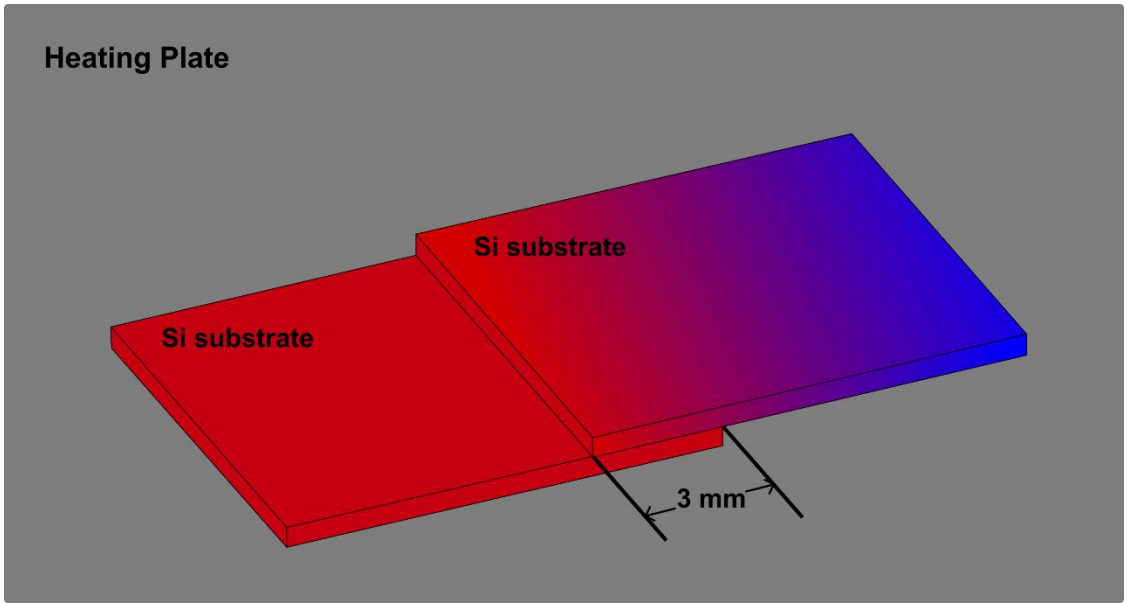

Fig S12. Temperature gradient Si substrate setup. The top Si chip (the PLD substrate) is elevated above the PLD heater to create a temperature gradient emanating from the contact point with the bottom chip. The chips were connected by silver paste.

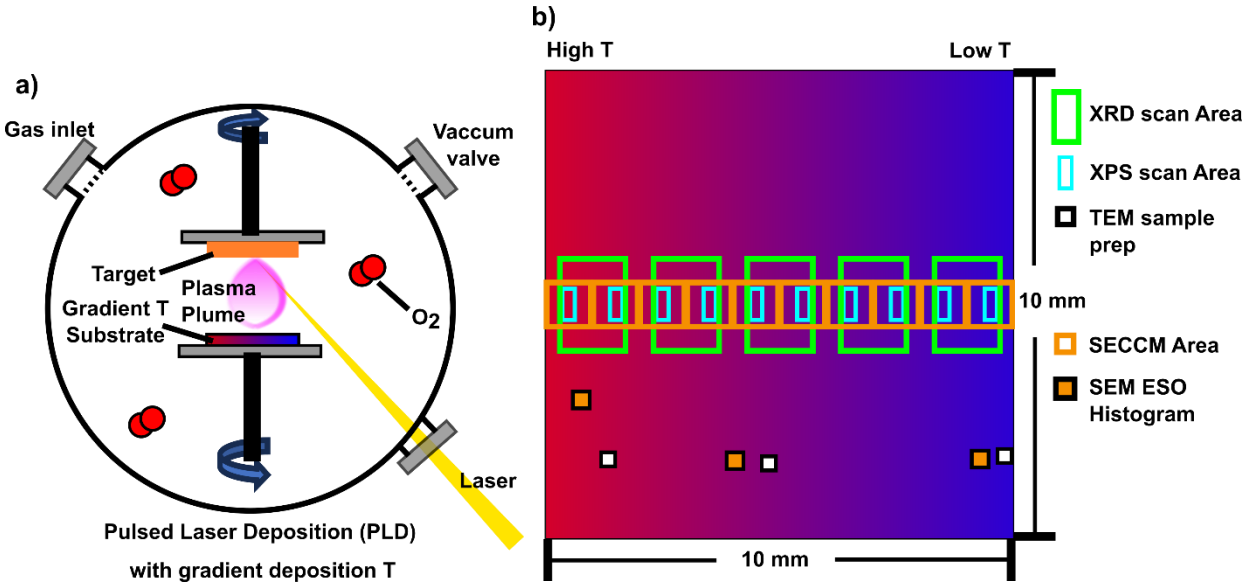

Fig. S13. Gradient substrate temperature PLD sample fabrication and characterization. (a) High-throughput electrode library synthesis using a lateral temperature gradient, and **(b)** characterization using spatially resolved XRD, XPS, SEM, SECCM, and STEM specimen preparation by FIB lift-out.

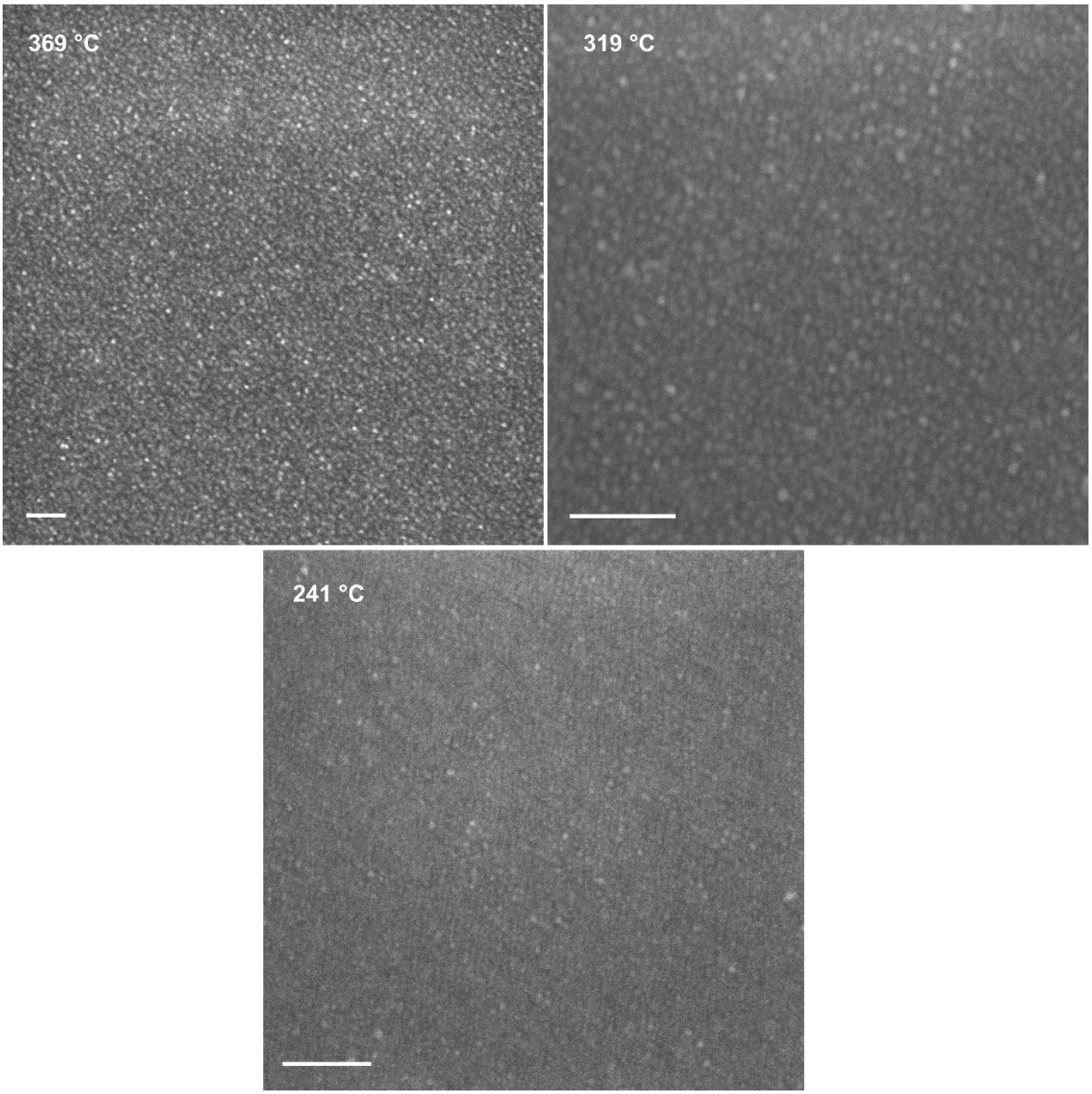

Fig. S14. SEM secondary electron images used for grain size measurement. The scale bar is 200 nm.

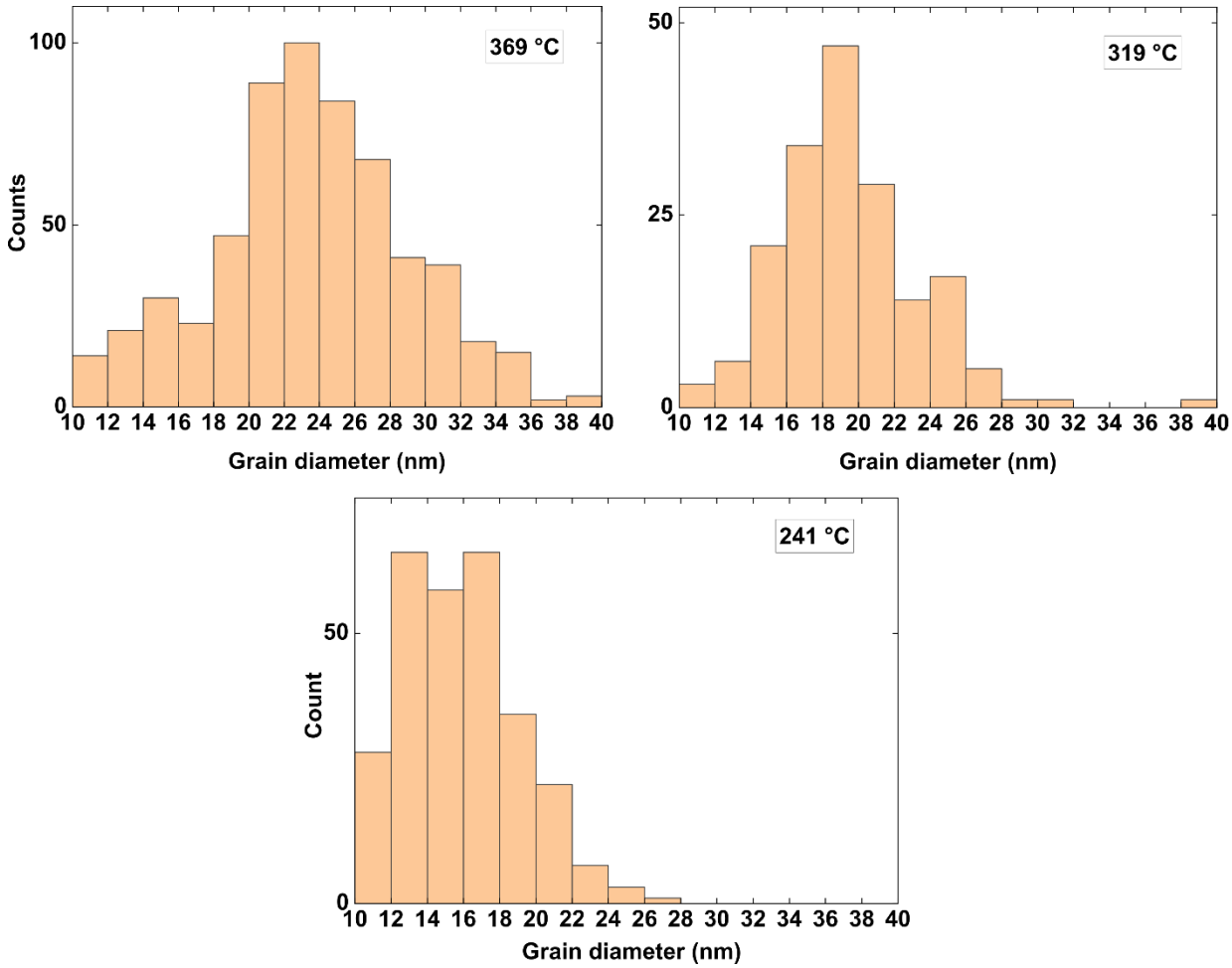

Fig. S15. ESO grain size at different deposition temperature measured from SEM images.

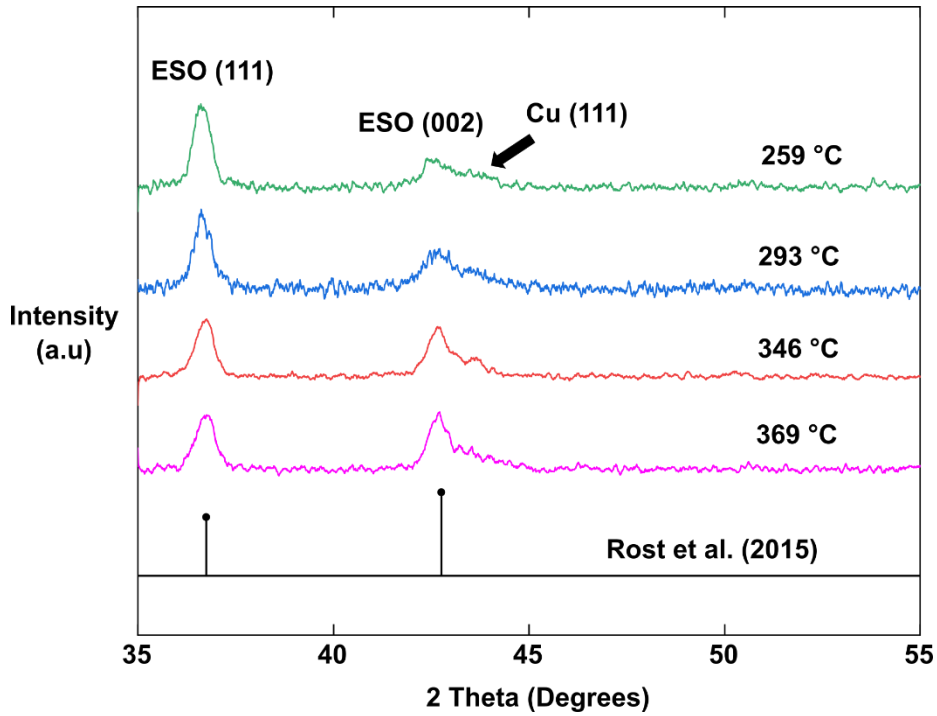

Fig. S16. **Tandem electrode XRD.** The ESO thin film grains have (111) texture at lower substrate temperatures and more random texture at higher temperatures. A randomly oriented polycrystalline rocksalt pattern shows the (002) peak intensity is greater than (111) in the un-textured case. XRD data from Rost et al.[38] is included.

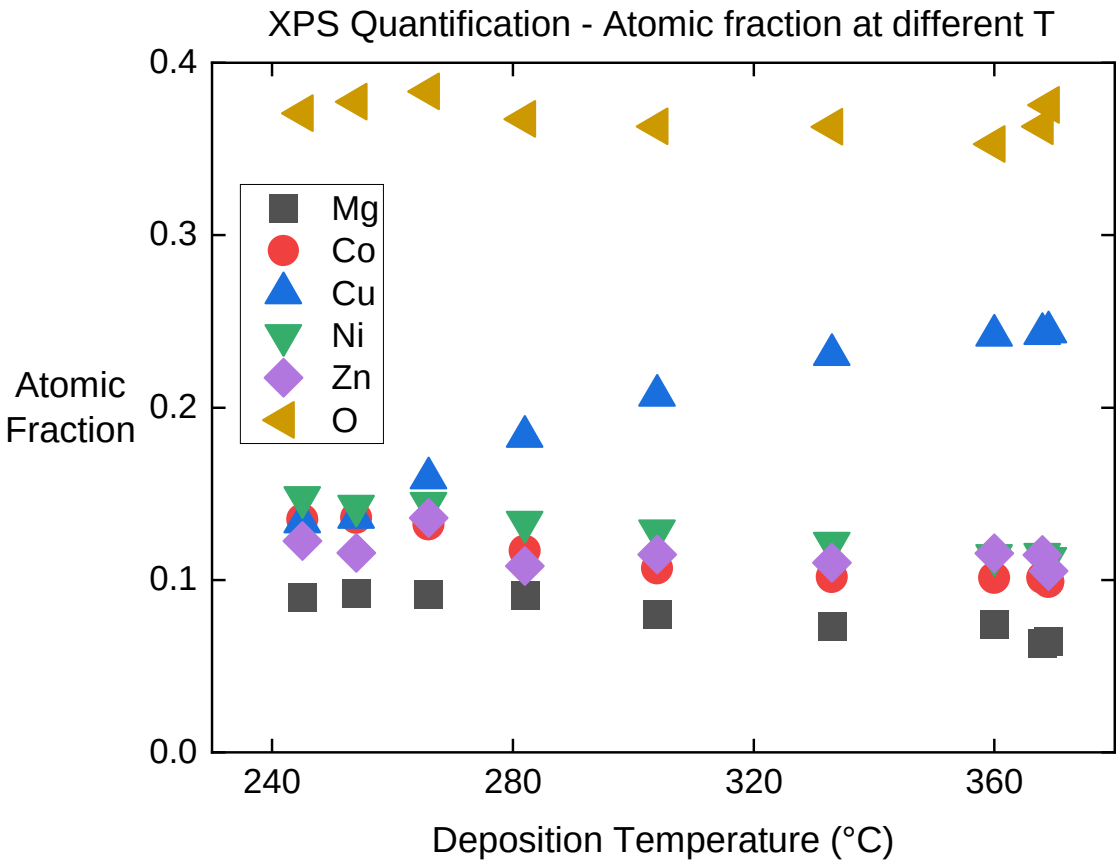

Fig. S17. **X-ray photoelectron spectroscopy (XPS) quantification of surface composition.** Sensitivity factor was acquired using XPS data of the PLD target as base to quantify and output compositional fraction of different species at different temperature location of gradient thin film tandem electrode.

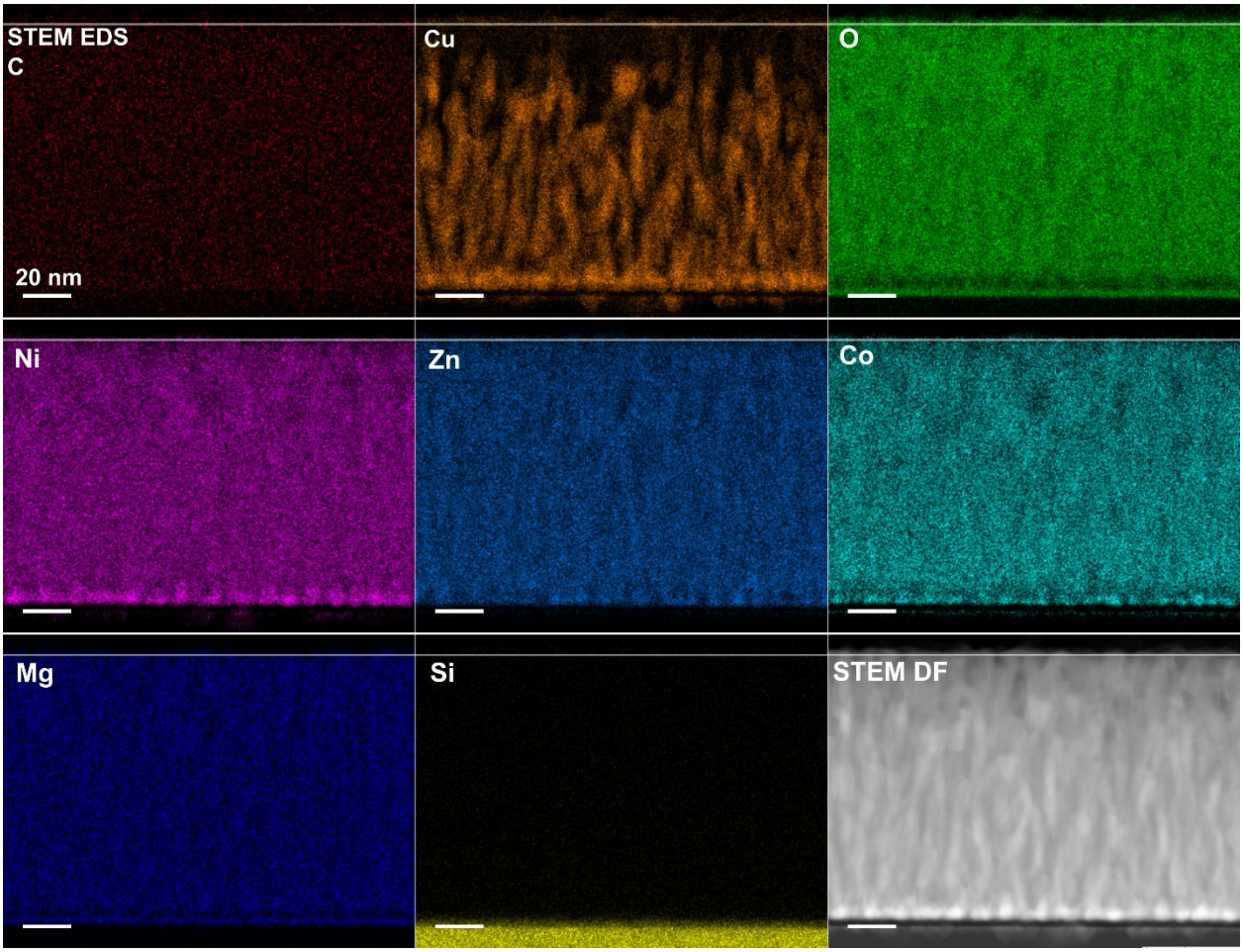

Fig. S18. STEM EDS of the location with substrate temperature 241 °C. White opaque lines indicate the film surface, where the oxygen signal intensity decreases to zero.

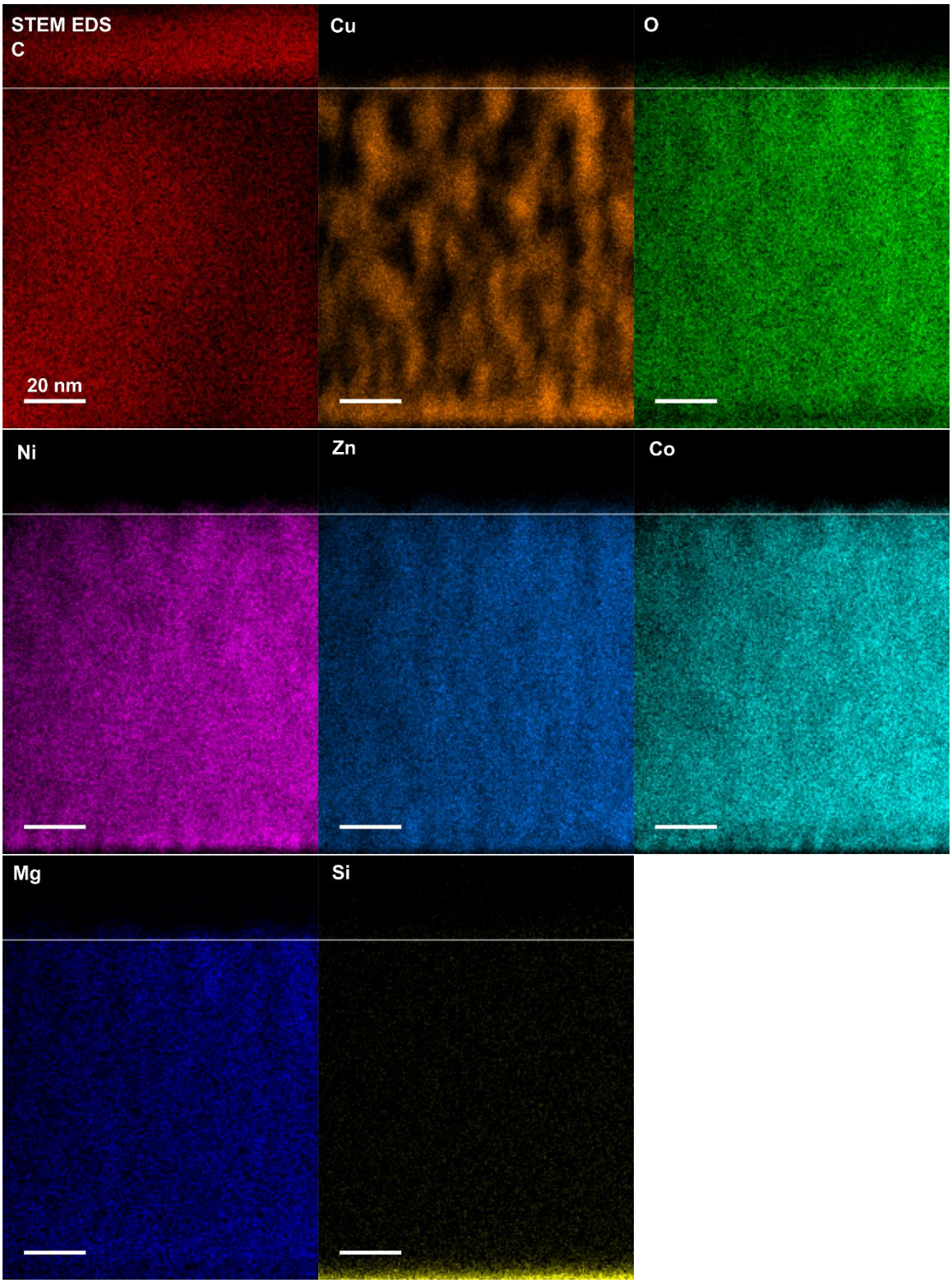

Fig. S19. STEM EDS of the location with substrate temperature 294 °C. White opaque lines indicate the film surface, where the oxygen signal intensity decreases to zero.

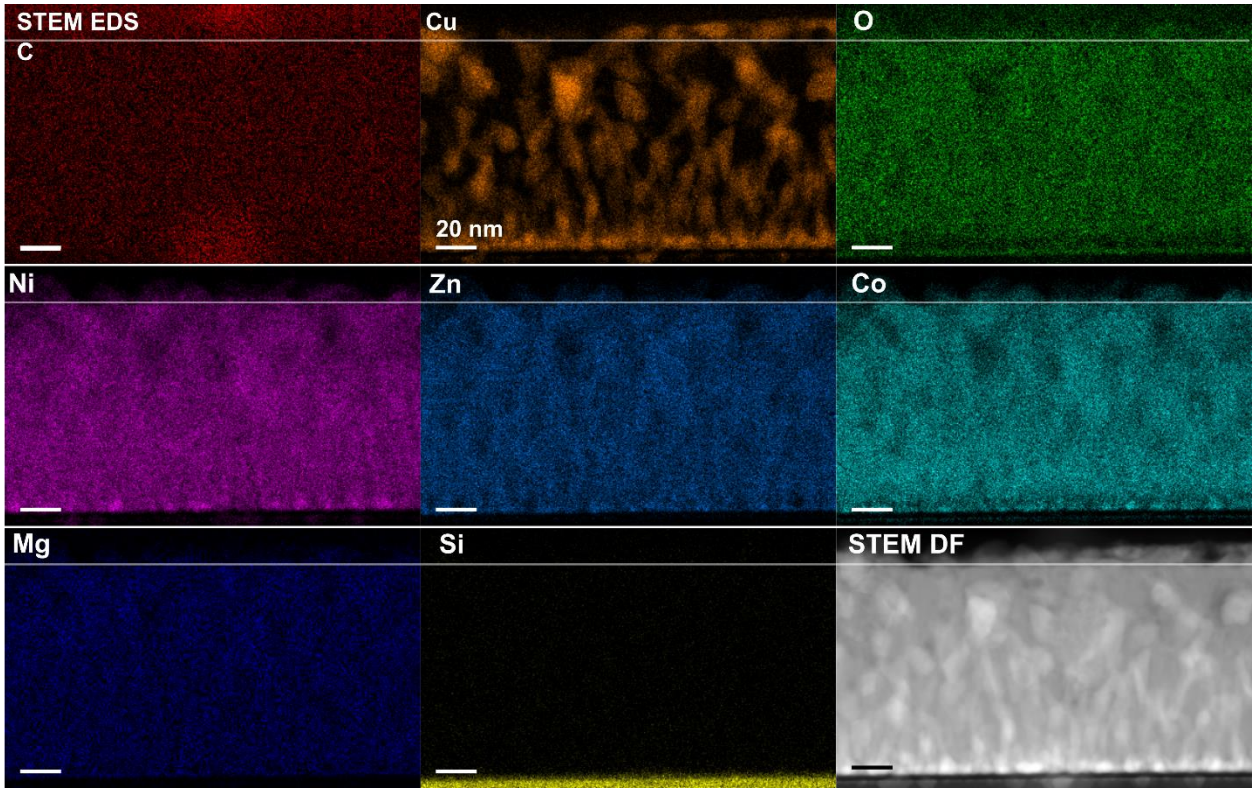

Fig. S20. STEM EDS of the location with substrate temperature 369 °C. White opaque lines indicate the film surface, where the oxygen signal intensity decreases to zero.

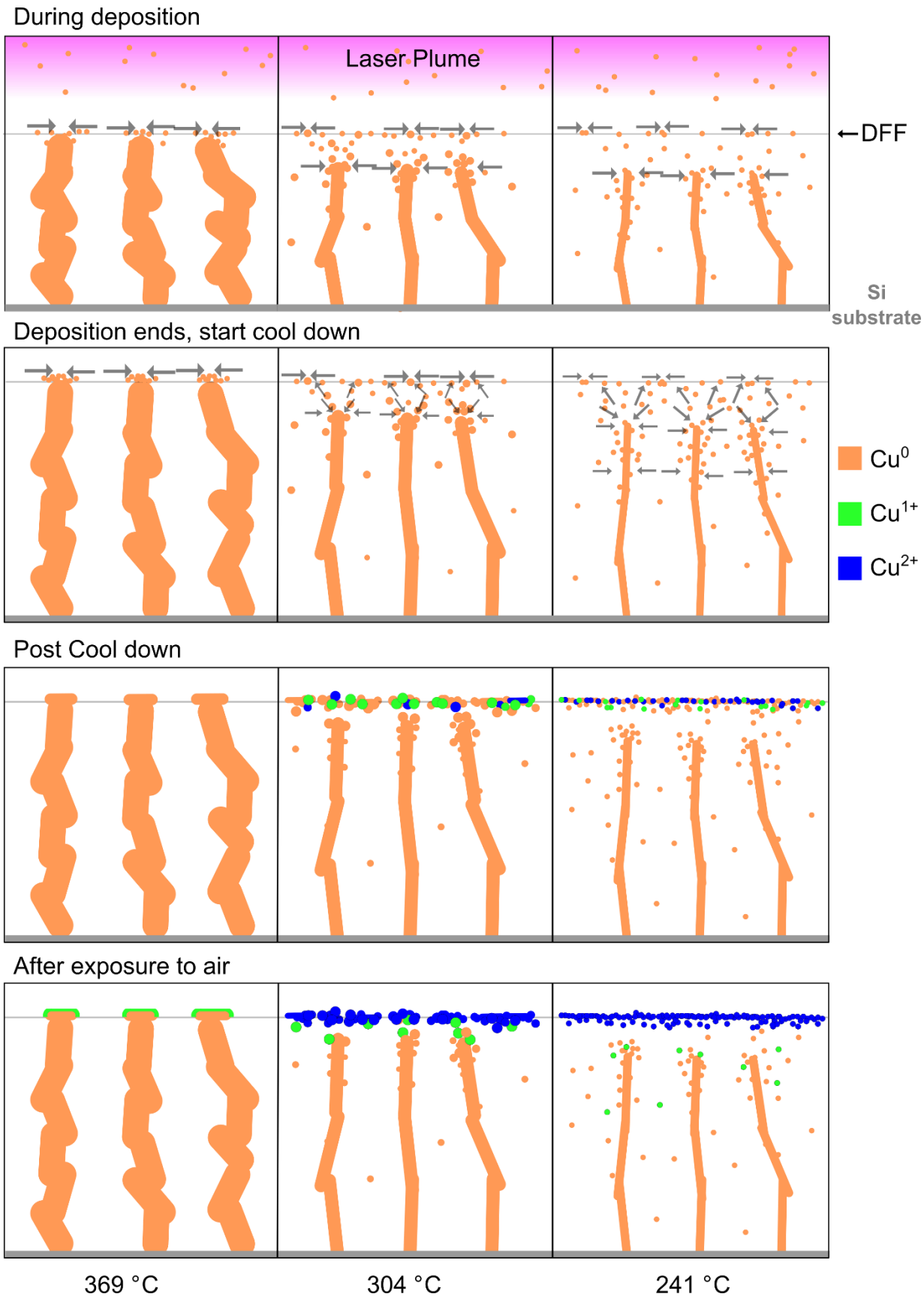
During deposition
Laser Plume
←DFF
Si substrate
Deposition ends, start cool down
Cu0
Cu1+
Cu2+
Post Cool down
After exposure to air
369 °C
304 °C
241 °C

Fig. S21. Hypothesized growth mechanism of Cu-ESO nanocomposite at different substrate temperatures and at various times during PLD synthesis. During deposition the deposition formation front (DFF) is moving away from the substrate. At the end of deposition, the substrate begins to cool to room temperature. The film rests at room temperature after cooling before it is removed from the PLD and exposed to air. In line with experimental observations, the final Cu distribution/morphology and valence depends on the local substrate temperature. At high temperatures (e.g., 369 °C) Cu adatoms diffuse rapidly along the surface and are incorporated into the Cu nanorods/structures at the DFF. After air exposure the relatively large Cu nanostructure/rod passivate by forming a small amount of Cu^{1+} (green). At intermediate and low temperatures (304 and 241 °C) Cu adatom surface diffusion is sluggish and limits incorporation of Cu into nanorods at the DFF. Unincorporated Cu thus remains in the subsurface and bulk diffusion is needed to incorporate them into the nanorods. Alternatively, they may diffuse to the film surface and exsolve as nanoparticles. Upon cooling and air exposure, these nanoparticles are oxidized to Cu^{1+} and Cu^{2+} (blue), with the extent of oxidation dependent on the particle size.

Experimental evidence supporting this Cu nanostructure formation mechanism, and specifically the sub-surface Cu depletion (**Fig. S21**, 304 °C and 241 °C), is the Cu elemental distribution measured by STEM EDS. Cation concentration profiles near the film surface at different substrate temperature locations show that the Cu concentration is close to or exceeded that of the ESO matrix Cu where the temperature was 369 °C (**Fig. S22a**, black dashed line). At lower substrate temperatures, the Cu concentration dips below that of the ESO matrix in the several nm below the film surface. This dip in near-surface Cu concentration relative to the ESO matrix is more significant at lower substrates temperatures, as depicted in **Fig. S21**. As mentioned, we hypothesize that Cu atoms/ions are diffusing to either the film surface or to the already formed Cu^0 nanostructure tips, yielding Cu depletion in the subsurface at lower PLD temperatures (**Fig. S22b**).

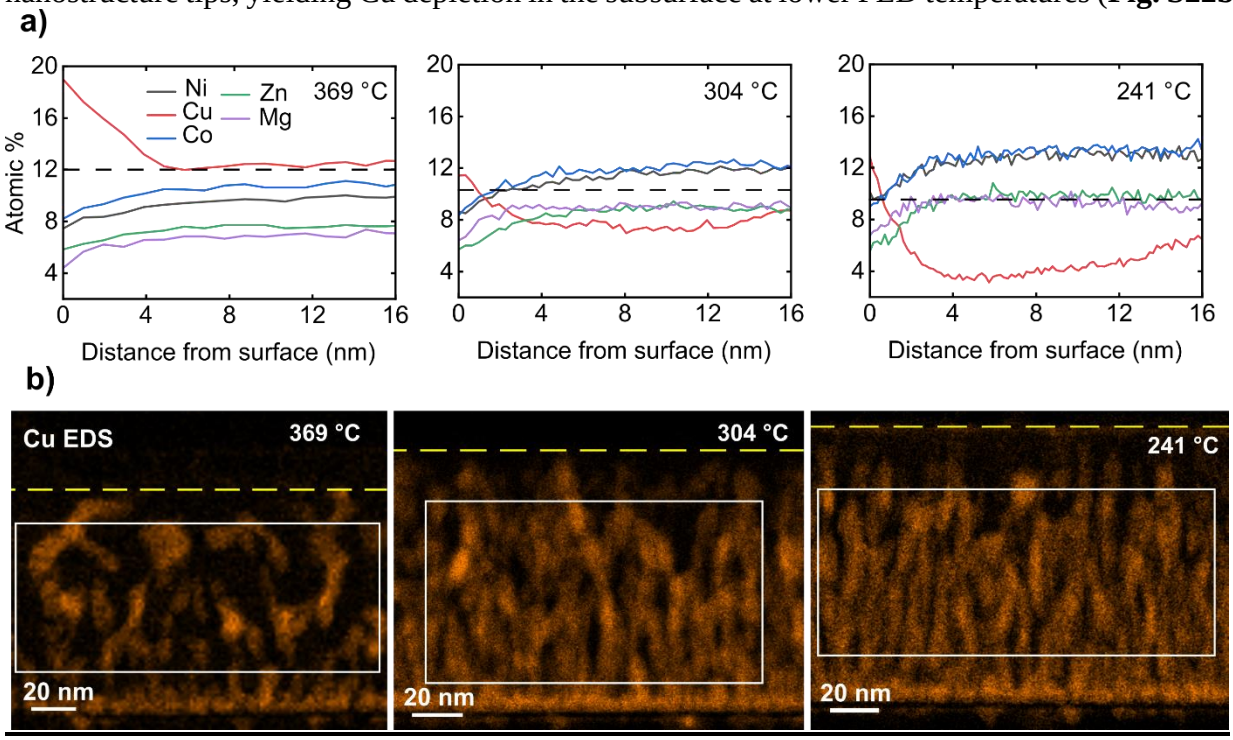

Fig. S22. Near-surface cation distribution shows Cu depletion at lower substrate temperatures. (a) Cation concentration profiles measured by STEM EDS near the tandem electrode surface at different substrate temperatures. Dashed black line indicates the nominal Cu concentration of the ESO matrix (calculated in the white boxes in **(b)**). **(b)** Cu L EDS signal at different substrate temperatures. White rectangles show where the nominal Cu concentration of the ESO matrix is determined. The yellow dashed line is the electrode surface position, as in **Fig. 4.**

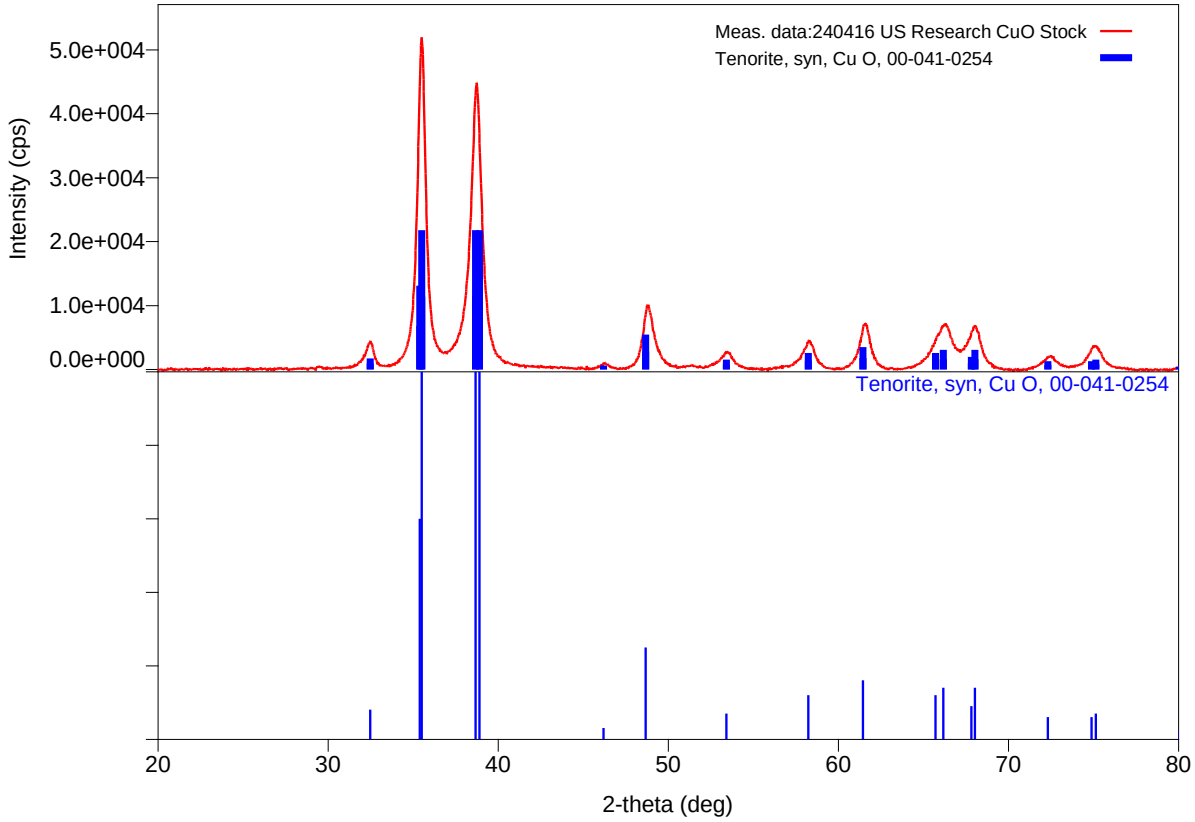

Fig. 23. XRD pattern of CuO nano particles used as a reference standard for EELS MLLS analysis (US Research nanomaterials, Inc.). Particles were used as Cu^{2+} reference EELS data.

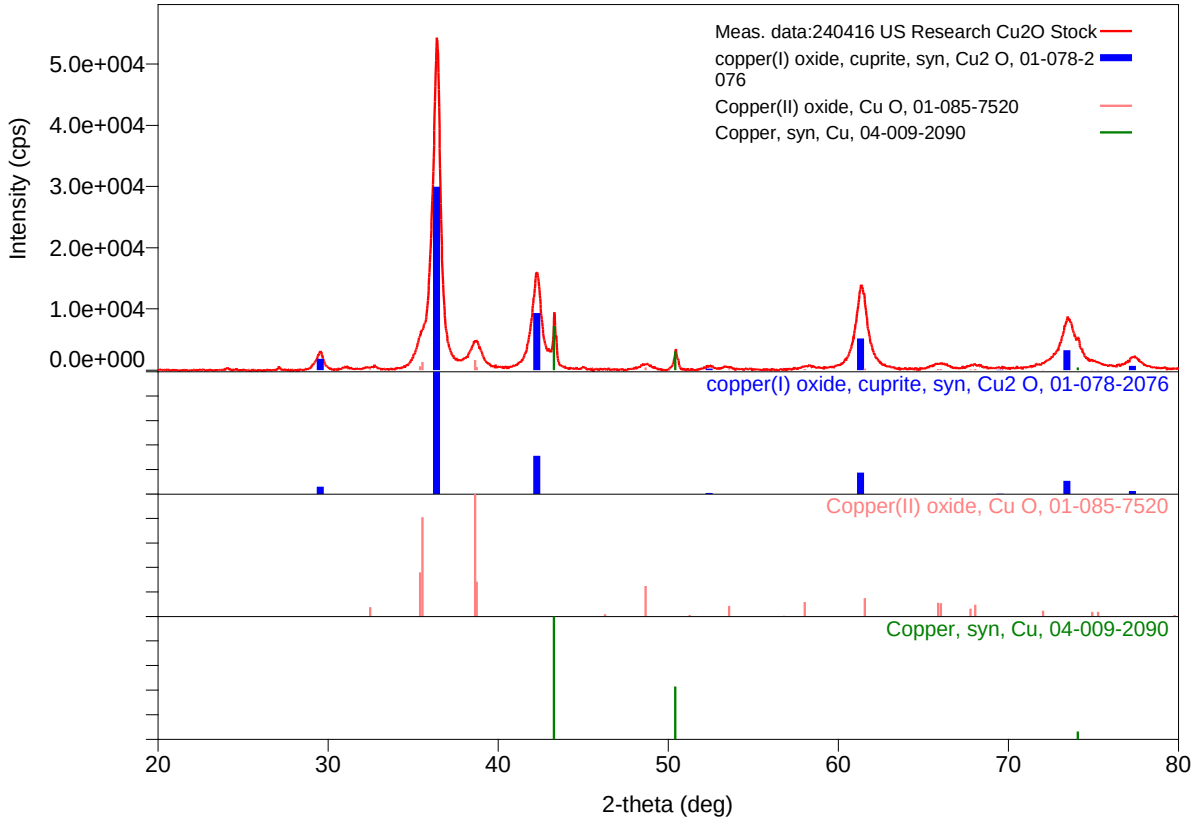

Fig. 24. XRD pattern of Cu_2O nano particles used as a reference standard for EELS MLLS analysis. Standard sample contains 81.7 mol % $Cu_2^{1+}O$, 13 mol % $Cu^{2+}O$, and 5.3 mol % Cu^0 assessed using Rietveld refinement quantitative analysis. US Research nanomaterials, Inc Product ID: US3075, CAS #: 1317-39-1.

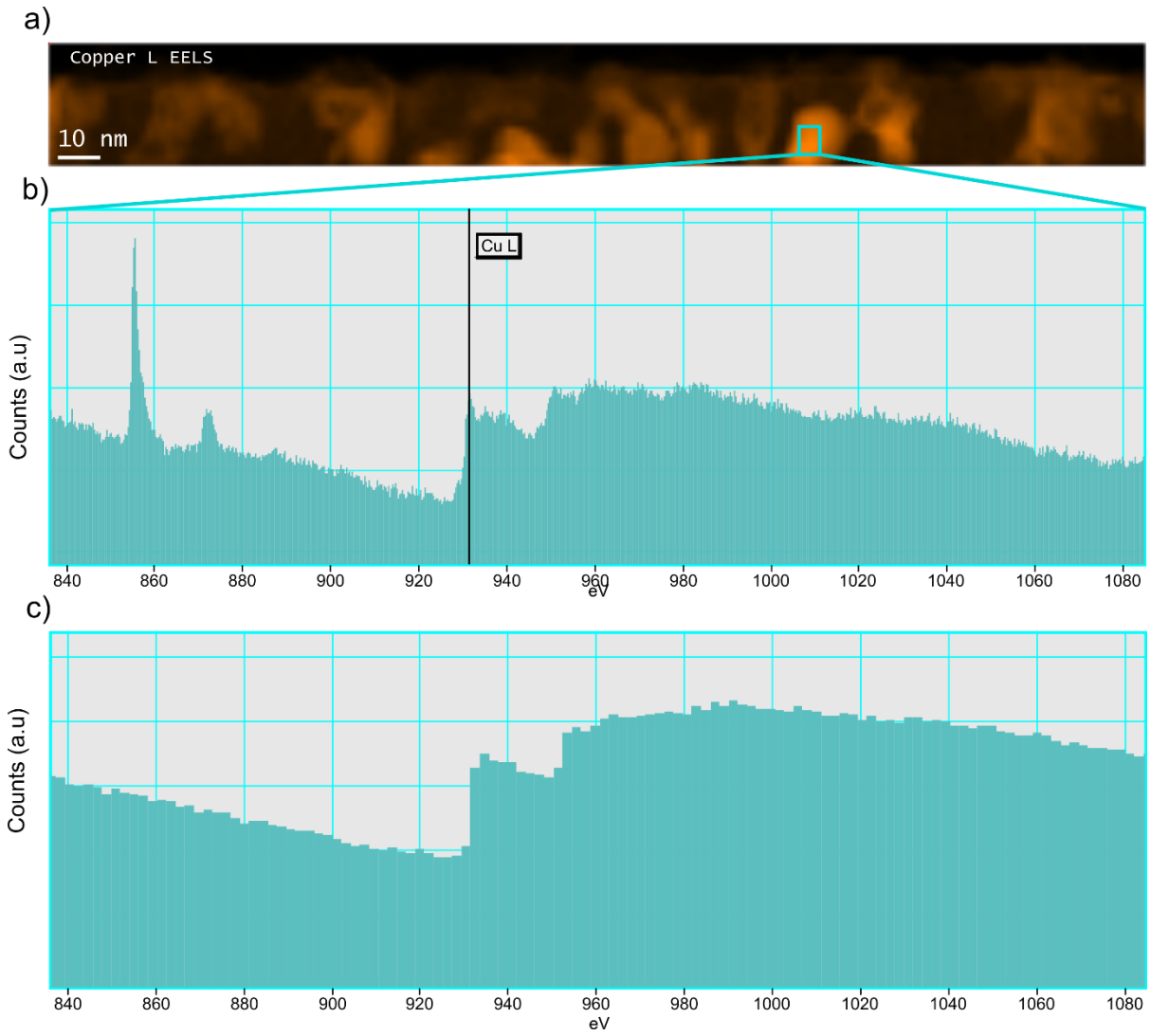

Fig. S25. Cu^0 EELS standard for MLLS fitting. (a) EELS Cu L map showing area over which where the Cu^0 standard spectrum was integrated. **(b)** Integrated EEL spectrum from location in **(a)**. **(c)** Cu^0 EELS from Gatan Atlas database.

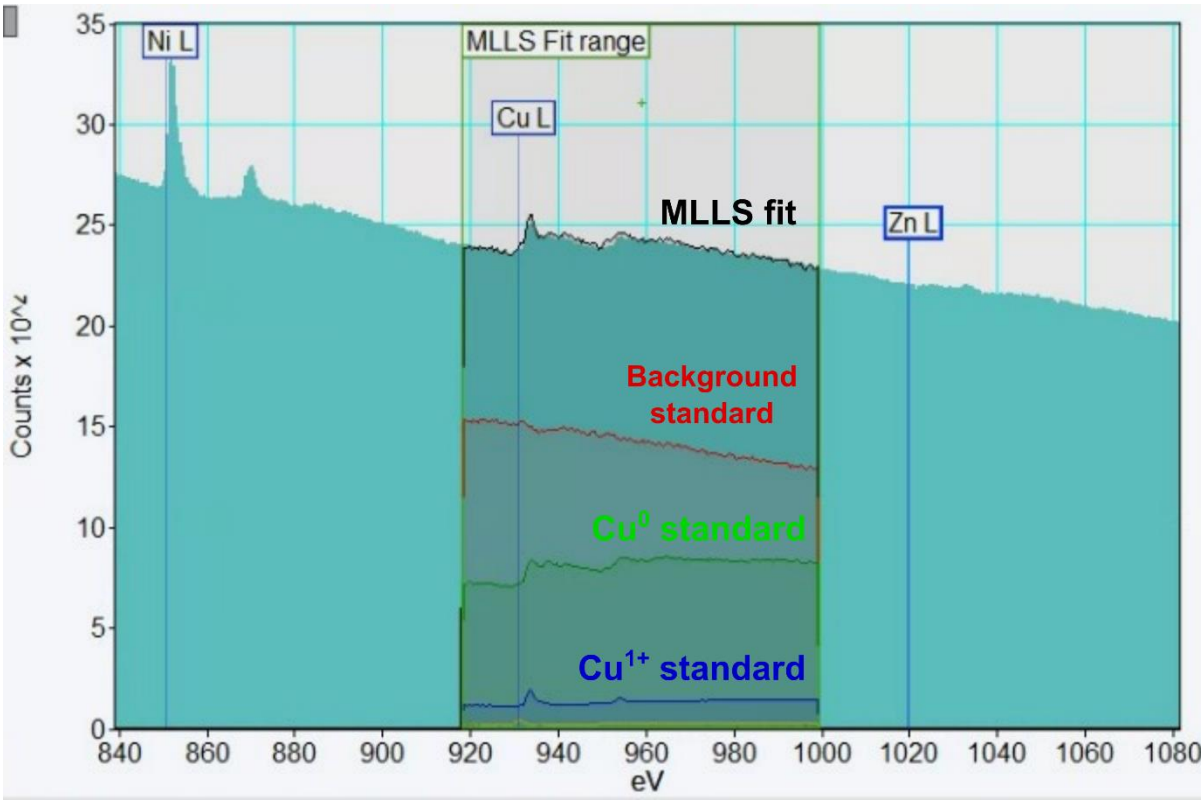

Fig. S26. Example MLLS fit of EELS recorded at the 369 °C location in the gradient sample. The MLLS fits the EELS spectrum well by combining $Cu^{1+}{}_2O$, Cu^0, and background standards.

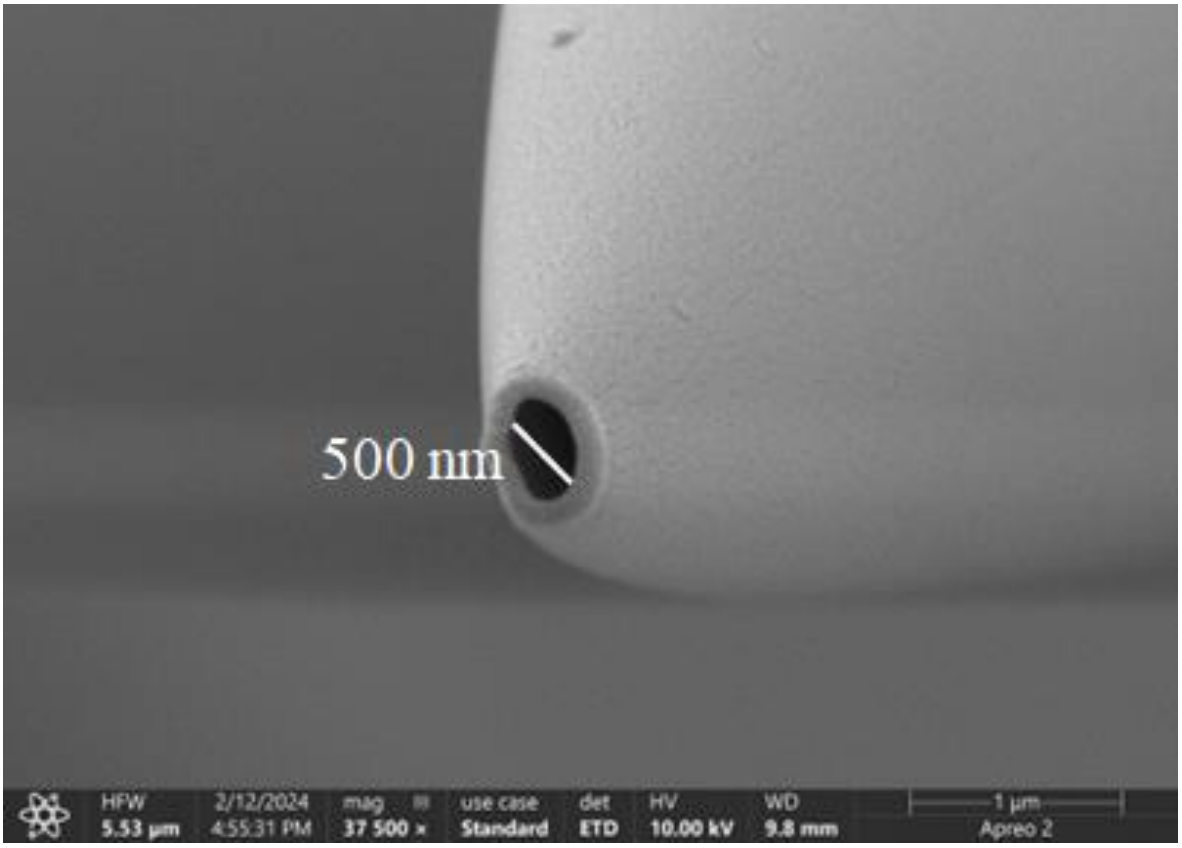

Fig. S27. SEM secondary electron image of SECCM nanopipette tip.

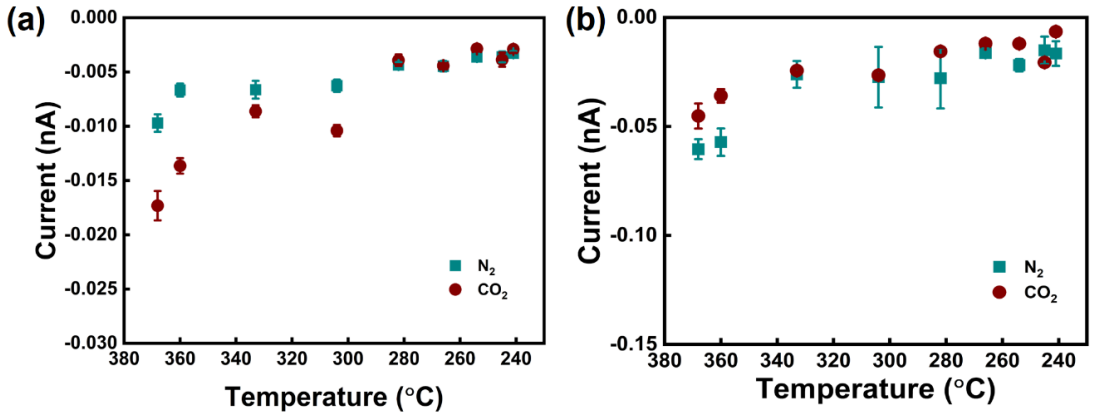

Fig. S28. Reduction current derived from voltammogram at two different potentials in N_2 and CO_2 atmosphere. (a) at -0.8 V and **(b)** at -1.1 V.

Supplemental References

1. Guo, H., Wang, X., Dupuy, A. D., Schoenung, J. M. & Bowman, W. J. Growth of nanoporous high-entropy oxide thin films by pulsed laser deposition. *Journal of Materials Research* **37**, 124–135 (2022).
2. Kresse, G. & Furthmüller, J. Efficient iterative schemes for ab initio total-energy calculations using a plane-wave basis set. *Physical Review B* **54**, 11169–11186 (1996).
3. Blöchl, P. E. Projector augmented-wave method. *Physical Review B* **50**, 17953–17979 (1994).
4. Perdew, J. P., Burke, K. & Ernzerhof, M. Generalized gradient approximation made simple. *Physical Review Letters* **77**, 3865–3868 (1996).
5. Ong, S. P. *et al.* Python Materials Genomics (pymatgen): A robust, open-source python library for materials analysis. *Computational Materials Science* **68**, 314–319 (2013).
6. Jain, A. *et al.* Commentary: The Materials Project: A materials genome approach to accelerating materials innovation. *APL Materials* **1**, 011002 (2013).
7. Horton, M. K., Montoya, J. H., Liu, M. & Persson, K. A. High-throughput prediction of the ground-state collinear magnetic order of inorganic materials using Density Functional Theory. *npj Comput Mater* **5**, 64 (2019).
8. Shanks, H. R., Maycock, P. D., Sidles, P. H. & Danielson, G. C. Thermal Conductivity of Silicon from 300 to 1400°K. *Phys. Rev.* **130**, 1743–1748 (1963).
9. Timans, P. J. Emissivity of silicon at elevated temperatures. *Journal of Applied Physics* **74**, 6353–6364 (1993).
10. Copper. *EELS.info* https://eels.info/atlas/copper (2015).

11. Kawasaki, S. *et al.* Photoelectrochemical water splitting enhanced by self-assembled metal nanopillars embedded in an oxide semiconductor photoelectrode. *Nat Commun* **7**, 11818 (2016).
12. Klinger, M. *CrysTBox - Crystallographic Toolbox*. (Institute of Physics of the Czech Academy of Sciences, Prague, 2015).
13. Roussigné, Y., Chérif, S. M., Stashkevich, A. A., Vidal, F. & Zheng, Y. Static and dynamic behavior of ultrathin cobalt nanowires embedded in transparent matrix. *Journal of Applied Physics* **118**, 233903 (2015).
14. Wang, X. & Wang, H. Recent Advances in Vertically Aligned Nanocomposites with Tunable Optical Anisotropy: Fundamentals and Beyond. *Chemosensors* **9**, 145 (2021).
15. Qian, D., Xu, B., Chi, M. & Shirley Meng, Y. Uncovering the roles of oxygen vacancies in cation migration in lithium excess layered oxides. *Physical Chemistry Chemical Physics* **16**, 14665–14668 (2014).
16. Wang, Z. L., Yin, J. S. & Jiang, Y. D. EELS analysis of cation valence states and oxygen vacancies in magnetic oxides. *Micron* **31**, 571–580 (2000).
17. Electron energy-loss near-edge structures of 3d transition metal oxides recorded at high-energy resolution. *Ultramicroscopy* **96**, 469–480 (2003).
18. Ikeno, H., Tanaka, I., Koyama, Y., Mizoguchi, T. & Ogasawara, K. First-principles multielectron calculations of Ni L2,3 NEXAFS and ELNES for LiNiO2 and related compounds. *Phys. Rev. B* **72**, 075123 (2005).
19. Spillane, L. *et al.* In-situ Oxidation State Mapping by Electron Energy-loss Spectroscopy. *Microscopy and Microanalysis* **26**, 1676–1677 (2020).

20. Zhang, W. *et al.* Exploring the Spatial Control of Topotactic Phase Transitions Using Vertically Oriented Epitaxial Interfaces. *Nano-Micro Lett.* **14**, 2 (2021).

21. Sassi, M. & Rosso, K. M. First principles simulations of MgO(100) surface hydration at ambient conditions. *Phys. Chem. Chem. Phys.* **26**, 2269–2276 (2024).

22. Koster, R. S., Fang, C. M., Dijkstra, M., Van Blaaderen, A. & Van Huis, M. A. Stabilization of Rock Salt ZnO Nanocrystals by Low-Energy Surfaces and Mg Additions: A First-Principles Study. *J. Phys. Chem. C* **119**, 5648–5656 (2015).

23. Wang, D. *et al.* Shape control of CoO and LiCoO2 nanocrystals. *Nano Res.* **3**, 1–7 (2010).

24. Youmbi, B. S. & Calvayrac, F. Structure of CoO(001) surface from DFT+U calculations. *Surface Science* **621**, 1–6 (2014).

25. Leonov, I. & Biermann, S. Electronic correlations at paramagnetic (001) and (110) NiO surfaces: Charge-transfer and Mott-Hubbard-type gaps at the surface and subsurface of (110) NiO. *Phys. Rev. B* **103**, 165108 (2021).

26. Xiang, J., Xiang, B. & Cui, X. NiO nanoparticle surface energy studies using first principles calculations. *New J. Chem.* **42**, 10791–10797 (2018).

27. Su, D., Xie, X., Dou, S. & Wang, G. CuO single crystal with exposed {001} facets - A highly efficient material for gas sensing and Li-ion battery applications. *Sci Rep* **4**, 5753 (2014).

28. Giese, D. R. Magnesium oxide (110) surface ordering (Order No. 3188391). Available from ProQuest Dissertations & Theses Global. (305386478). Retrieved from https://www.proquest.com/dissertations-theses/magnesium-oxide-110-surface-ordering/docview/305386478/se-2.

29. Mishra, A. K., Roldan, A. & De Leeuw, N. H. CuO Surfaces and CO_2 Activation: A Dispersion-Corrected DFT+ *U* Study. *J. Phys. Chem. C* **120**, 2198–2214 (2016).

30. Vahidi, H. *et al.* Reversible Enhancement of Electronic Conduction Caused by Phase Transformation and Interfacial Segregation in an Entropy-Stabilized Oxide. *Adv Funct Materials* 2315895 (2024) doi:10.1002/adfm.202315895.

31. Balcerzak, M., Kawamura, K., Bobrowski, R., Rutkowski, P. & Brylewski, T. Mechanochemical Synthesis of (Co,Cu,Mg,Ni,Zn)O High-Entropy Oxide and Its Physicochemical Properties. *J. Electron. Mater.* **48**, 7105–7113 (2019).

32. Jacobson, V. *et al.* The role of Co valence in charge transport in the entropy-stabilized oxide (Mg0.2Co0.2Ni0.2Cu0.2Zn0.2)O. *Journal of the American Ceramic Society* **106**, 1531–1539 (2023).

33. Huang, K., Lee, H. Y. & Goodenough, J. B. Sr- and Ni-Doped LaCoO3 and LaFeO3 Perovskites: New Cathode Materials for Solid-Oxide Fuel Cells. *J. Electrochem. Soc.* **145**, 3220 (1998).

34. Qiao, L. & Bi, X. Direct observation of Ni3+ and Ni2+ in correlated LaNiO3−δ films. *EPL* **93**, 57002 (2011).

35. Señarís-Rodríguez, M. A. & Goodenough, J. B. LaCoO3 Revisited. *Journal of Solid State Chemistry* **116**, 224–231 (1995).

36. Goodenough, J. B. & Raccah, P. M. Complex vs Band Formation in Perovskite Oxides. *Journal of Applied Physics* **36**, 1031–1032 (1965).

37. Chae, S., Williams, L., Lee, J., Heron, J. T. & Kioupakis, E. Effects of local compositional and structural disorder on vacancy formation in entropy-stabilized oxides from first-principles. *npj Comput Mater* **8**, 1–7 (2022).

518 38. Rost, C. M. *et al.* Entropy-stabilized oxides. *Nat Commun* **6**, 8485 (2015).

519